COMPLEX FILTERS AS A CASCADE OF BUFFERED GINGELL STRUCTURES: DESIGN FROM BAND-STOP CONSTRAINTS

A Thesis
presented to
the Faculty of California Polytechnic State University,
San Luis Obispo

In Partial Fulfillment
of the Requirements for the Degree
Master of Science in Electrical Engineering

by
Samuel Robert Johnston
June 2016

COMMITTEE MEMBERSHIP

TITLE: Complex Filters as a Cascade of Buffered Gingell Structures: Design from Band-Stop Constraints

AUTHOR: Samuel Robert Johnston

DATE SUBMITTED: June 2016

COMMITTEE CHAIR: Vladimir Prodanov, Ph.D.
Associate Professor of Electrical Engineering

COMMITTEE MEMBER: David Braun, Ph.D.
Professor of Electrical Engineering

COMMITTEE MEMBER: Wayne Pilkington, Ph.D.
Associate Professor of Electrical Engineering

ABSTRACT

Complex Filters as a Cascade of Buffered Gingell Structures: Design from Band-Stop Constraints

Samuel Robert Johnston

This thesis presents an active Complex Filter implementation that creates a transfer function with a single real pole and a complex zero. The two-input/two-output network developed in this thesis responds differently based upon the relative phase difference of the two inputs. If a negative ninety-degree phase difference occurs between the two inputs, the filter exhibits a bandstop response. While a positive ninety-degree phase difference exhibits a bandpass response. This topology relates to Gingell's RC-CR polyphase topology but because of the use of op-amps, can cascaded without suffering loading effects. This thesis focuses primarily on the bandstop response characteristics of the filter. In a several stage cascade, each stage contributes a notch to broaden the attenuation band. Closed form design equations were derived to give expressions for the "attenuation floor". These equations predict the attenuation provided by a cascaded system. The closed form expressions derived in this thesis implement an example five-stage topology that operates from 147 Hz to 3.34 KHz. The thesis also investigates the robustness of multi-stage cascades to component variations. Monte Carlo analysis determines the effects of cascading the filter in different orders, component tolerances, and a comparison to an idealized polyphase RC-CR topology.

Keywords: Complex Filters, image rejection, phase splitter, quadrature, active network, cascade

TABLE OF CONTENTS

Page

LIST OF TABLES

Table Page

LIST OF FIGURES

Figure Page

1. INTRODUCTION

1.1. Thesis Statement

Two active components implement a buffered first order Gingell network. Each stage contributes a single real pole and a single complex zero with the same magnitude. Per-stage buffering offers benefits in the design of achievable attenuation and flexibility in stage ordering. N filter stages have N-factorial different network configurations; some connection configurations have a greater robustness to component variations than others.

1.2. Statement of Problem

This thesis designs and implements an active complex filter that creates a transfer function with a single real pole and complex zero. This topology derives from an RC-CR topology, but creates more complex transfer functions through cascading.

1.3. Purpose of Study

This study creates an active Complex Filter based upon an RC network developed by Gingell [1]. Upon verification of the new topology, the discussion shifts to the cascading properties of the topology

This thesis investigates the number of active devices needed to create an active implementation of the Gingell network. An active implementation drives subsequent stages without experiencing loading effects. An N^{th} order filter network has N! different arrangements even though the resulting transfer function remains unchanged. Different cascade configurations attempt to improve system robustness.

The topic of designing a cascaded complex network and the parameters needed for characterization become a major focus of this thesis. Bandwidth and attenuation seen in the stopband characterize the system response. Closed-form expressions approximate attenuation and bandwidth based upon frequency selection.

1.4. Differential Circuits (Multi-input Networks) and Their Relation to Complex Circuits

To better understand Complex Filters, this section presents an overview of traditional multi-input/multi-output networks that operate on conceptually similar principals.

Differential amplifiers are an example of a 2-input linear network. A differential amplifier requires two responses for characterization: common-mode and differential-mode characteristics [2].

To obtain common-mode characteristics, drive each input of the amplifier with signals that have the same magnitude and a 0-degree phase difference; short the two inputs of the amplifier and driving both inputs with the same signal. Figure 1 demonstrates conceptually the Common-mode response of a differential amplifier.

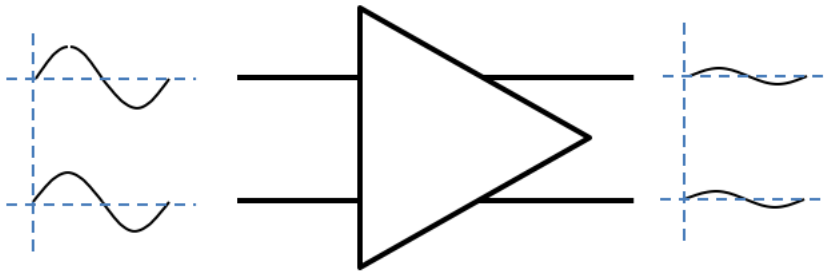

Figure 1. Common-mode characteristics of a differential amplifier

The common mode gain approximately zero; $A_{CM} \sim 0$. In an ideal amplifier, $A_{CM} = 0$ [2].

Differential-mode characteristics result from driving each input of the amplifier with signals that have the same magnitude and a 180-degrees phase difference. When one input gets larger, the other gets smaller. Unlike the common-mode characteristics, desired differential gain is large; $A_{DM} >> A_{CM}$.

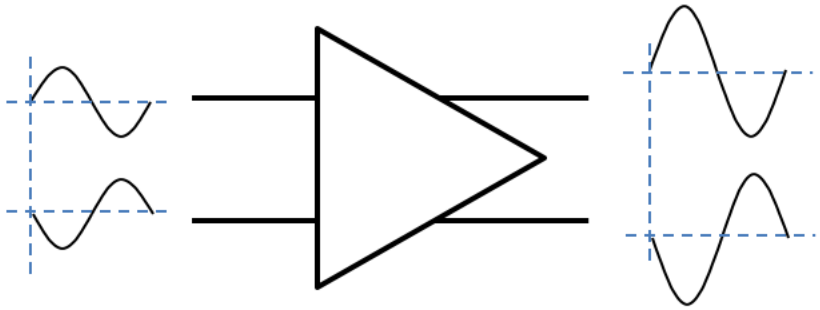

Figure 2. Differential-mode characteristics of a differential amplifier

Common mode rejection ration (CMRR) measures how well the amplifier rejects common-mode input voltage compared to differential-input voltage:

$$CMRR = \left|\frac{A_{DM}}{A_{CM}}\right| \tag{1.1}$$

where

$$A_{DM} = differential - mode\ voltage\ gain$$
$$A_{CM} = common - mode\ voltage\ gain$$

This work considers a 2-input/2-output network that discriminates signals based upon input frequency and the relative phase difference between inputs.

The adjective "complex" refers to the ability of the network to simultaneously receive two input signals and deliver two output signals. A pair of (scalar) signals can be regarded as a vector or a complex quantity; Appendix A contains a discussion on this

topic [3]. Complex filters discriminate (complex) signals based upon the relative phase difference of the signals applied to the two inputs. Two frequency responses characterize these filters: “negative frequency” response and the “positive frequency” response; Appendix B discusses the topic of positive and negative frequencies. The two test signals in a complex filter maintain a positive and negative 90-degree phase shift.

Characterizing a Complex Filter requires quadrature input signals [3]. Looking at what signal leads and lags relative to the other signal determines filter performance.

When the first signal lags the second (Figure 3), a negative sequence input, the filter rejects this sequence. This performance is similar to the common-mode characteristics of the differential amplifier.

For determining the “negative frequency” response, a negative 90-degree phase difference occurs between the two input signals.

$$input\ 1 = \frac{A}{\sqrt{2}}\cos(\omega t) \Longrightarrow \frac{A}{\sqrt{2}} \tag{1.2}$$

$$input\ 2 = -\frac{A}{\sqrt{2}}\sin(\omega t) \Longrightarrow j\frac{A}{\sqrt{2}} \tag{1.3}$$

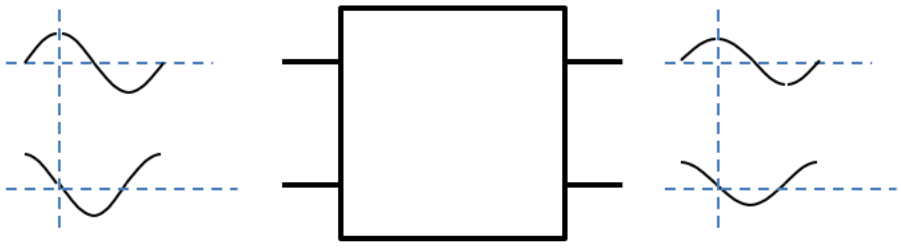

Figure 3. Complex Filter when inputs correspond to a negative sequence – Attenuate inputs

When the first signal leads the second (Figure 4), a positive sequence input, the filter passes this sequence with a given amount of gain. This performance resembles the differential-mode characteristics of a differential amplifier.

For determining "positive frequency" response, a positive 90-degree phase difference occurs between the two inputs:

$$input\ 1 = \frac{A}{\sqrt{2}}\cos(\omega t) \implies \frac{A}{\sqrt{2}} \tag{1.4}$$

$$input\ 2 = \sin(\omega t) \implies -j\frac{A}{\sqrt{2}} \tag{1.5}$$

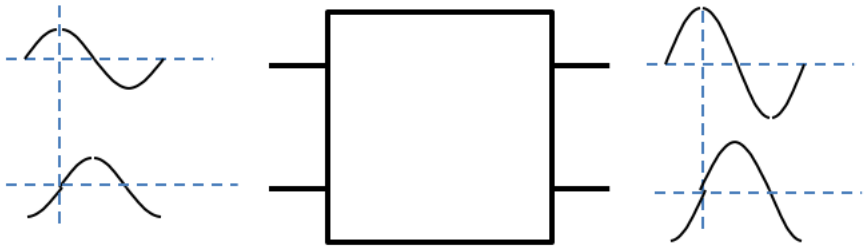

Figure 4. Complex Filter when inputs correspond to a positive sequence – Exhibit gain

1.5. Gingell Topology

An RLC notch filter has a frequency symmetric response. This differs from the frequency asymmetric response found in a Complex Filter. Deriving the RCL notch filter response shows the creation of a frequency symmetric response. Figure 5 shows a single stage notch filter. Performing the derivation of the RLC notch filter serves as an introduction to the importance of transmission zeroes in signal rejection.

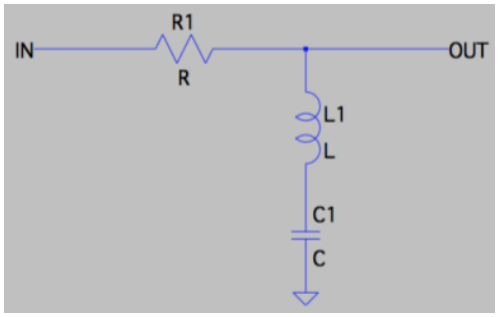

Figure 5. Single stage RLC notch filter

Figure 5 and equations (1.6)-(1.9) derive the transfer function for an RLC notch filter.

$$H(s) = \frac{Z_{LC}}{Z_{LC} + R} \tag{1.6}$$

$$H(s) = \frac{\frac{s^2CL + 1}{sC}}{\frac{s^2CL + 1}{sC} + R} \tag{1.7}$$

$$H(s) = \frac{s^2CL + 1}{s^2CL + sCR + 1} \tag{1.8}$$

$$H(s) = \frac{s^2 + \frac{1}{LC}}{s^2 + \frac{sR}{L} + \frac{1}{LC}} \tag{1.9}$$

This RLC notch filter response has two poles and two zeros; corresponding to a second order system. A voltage divider between the series combination of the inductor and capacitor with the resistor gives the transfer function for the filter.

The zeros locations correspond to $\pm j\frac{1}{\sqrt{LC}}$. Having zeros on the jω axis creates the notch response.

Find pole locations utilize the denominator of transfer function of the standard RLC notch filter, Equation (1.10). This discussion assumes a critically damped system; resulting in two real poles.

$$s^2 + \frac{R}{L}s + \frac{1}{LC} = 0 \tag{1.10}$$

$$(s + \omega_p)\left(s + \omega_p\right) = 0 \tag{1.11}$$

$$s^2 + 2 * s * \omega_p + {\omega_p}^2 \tag{1.12}$$

$$2 * \frac{1}{\sqrt{LC}} = \frac{R}{L} \tag{1.13}$$

$$R = 2 * \sqrt{\frac{L}{C}} \tag{1.14}$$

Insert (1.14) into (1.10):

$$s^2 + \frac{1}{L} * s * 2\sqrt{\frac{L}{C}} * + \frac{1}{LC} = 0 \tag{1.15}$$

$$(s + \frac{1}{\sqrt{LC}})(s + \frac{1}{\sqrt{LC}}) \tag{1.16}$$

This circuit creates two identical poles located at $\frac{-1}{\sqrt{LC}}$.

The symmetric zero arrangement (Figure 6, a) produces a symmetric response with respect to the origin. The filter has identical responses for both positive and negative frequencies. Due to this symmetric frequency response, the standard RLC notch is not a complex filter.

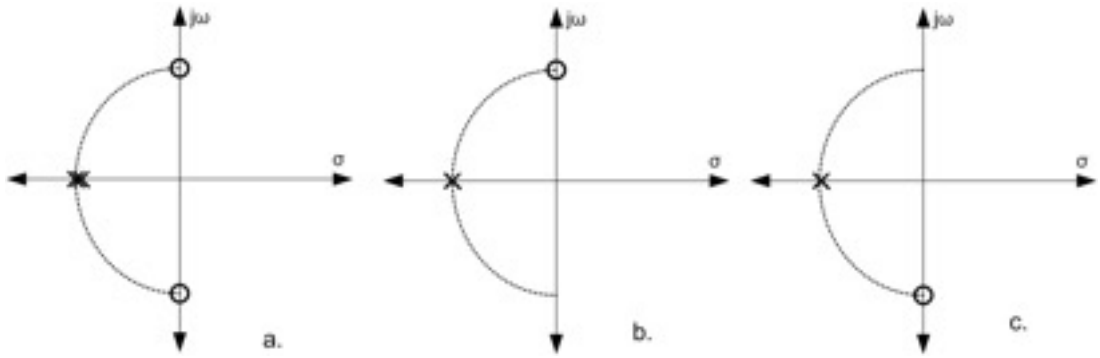

Figure 6. (a) symmetric pole-zero plot, RLC notch filter, (b) single real pole and imaginary zero, asymmetrical response, (c) single real pole and negative imaginary zero, asymmetrical response

To create a complex filter, the system needs to have an asymmetric pole zero response. For example, the pole zero diagram in Figure 6,b implements a transfer function that has a single real pole and a single imaginary zero. Figure 6,c implements a transfer function that has a single real pole and a single negative imaginary zero. This filter has a band-stop response with negative input sequence and a band-pass response with positive input sequence.

The RC Ladder network developed by Gingell, Figure 7, [1] implements a transfer function that has a single real pole and a single complex zero under quadrature drive. Unlike the complex filter structures discussed in Chapter 3, the Gingell topology is a 4-input/4-output complex network. This topology accepts four signals 90-degrees out of phase with each other and produces four signals 90-degrees out of phase with each other.

This network essentially behaves as two 2-input/2-output networks connected on top of each other.

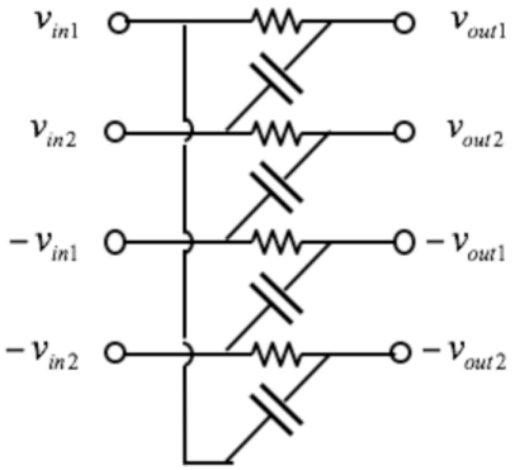

Figure 7. Gingell Topology – RC Ladder Network [1]

Gingell's a 4-input/4-output creates fully differential complex filter.

Equations (1.17) and (1.18) give the transfer function of the Gingell network:

$$V_{out1} = \frac{1}{sCR+1}V_{in1} + \frac{sCR}{sCR+1}V_{in2} \tag{1.17}$$

$$V_{out2} = -\frac{sCR}{sCR+1}V_{in1} + \frac{1}{sCR+1}V_{in2} \tag{1.18}$$

This network creates the pole-zero response shown in Figure 6,c.

The Gingell network creates the desired asymmetric pole zero response and reacts differently to positive and negative frequency. Gingell's network (Figure 7) is passive. If one attempts to connect multiple stages of the passive network, the overall response becomes loaded. Zero locations remain the same but pole locations shift.

Examining the effect of positive and negative frequencies on the transfer function illustrates the frequency asymmetric response of the Gingell topology.

Consider an input sequence with positive frequency:

$$V_{in1}(t) = \cos(\omega t) \tag{1.19}$$

$$V_{in2}(t) = \sin(\omega t) \tag{1.20}$$

In the phasor domain, this sequence becomes:

$$V_{in1} = 1 \tag{1.21}$$

$$V_{in2} = -\mathrm{j} \tag{1.22}$$

Evaluating equations 1.17 and 1.18 using 1.21 and 1.22 as inputs yields the following response:

$$V_{in1} = 1 * \frac{1 + \omega * RC}{1 + j * \omega * R * C} \tag{1.23}$$

$$V_{in1} = -j * \frac{1 + \omega * RC}{1 + j * \omega * R * C} \tag{1.24}$$

This shows that an input sequence of (1, -j) maintains the same phase shift on the output.

The magnitude of the system with a positive input sequence:

$$|H_{+\omega}| = \frac{|1 + \omega * RC|}{\sqrt{1 + (\omega * R * C)^2}} \tag{1.25}$$

The magnitude response of the system is greater than or equal to one for all frequencies. The maximum value of this magnitude response occurs at the characteristic frequency reciprocally related to the time-constant RC. At the characteristic frequency, $|H_{+\omega}| = \sqrt{2}$; this corresponds to a +3dB gain in the logarithmic scale.

Now consider an input sequence with negative frequency:

$$V_{in1}(t) = \cos(\omega t) \tag{1.26}$$

$$V_{in2}(t) = -\sin(\omega t) \tag{1.27}$$

In the phasor domain, this sequence becomes:

$$V_{in1} = 1 \tag{1.28}$$

$$V_{in2} = \mathrm{j} \tag{1.29}$$

Evaluating equations 1.17 and 1.18 using 1.28 and 1.29 as inputs yields the following response:

$$V_{in1} = 1 * \frac{1 - \omega * RC}{1 + j * \omega * R * C} \tag{1.30}$$

$$V_{in1} = j * \frac{1 - \omega * RC}{1 + j * \omega * R * C} \tag{1.31}$$

An input sequence of type (1, j) produces an output sequence of the same type.

The above derivation shows the Gingell topology maintains the relative phase differences on the input.

The magnitude of the system with a negative input sequence becomes:

$$|H_{-\omega}| = \frac{|1 - \omega * RC|}{\sqrt{1 + (\omega * R * C)^2}} \tag{1.32}$$

The system yields a magnitude response less than or equal to one for all frequencies. At the characteristic frequency, $|H_{-\omega}| = 0$. In the logarithmic scale, a magnitude of 0 corresponds to $-\infty$ at the characteristic frequency. As predicted, a negative-frequency sequence creates the notch response.

1.6. Cascaded Gingell Topology Implementations

This thesis creates an active implementation of the Gingell topology that maintains the same transfer function and exhibits cascade-able properties. Figure 8 shows an active implementation of the Gingell topology. This topology connects a unity gain buffer to each output of the network shown in Figure 7. This active network requires four active components, and maintains the fully differential aspects of Gingell's complex topology.

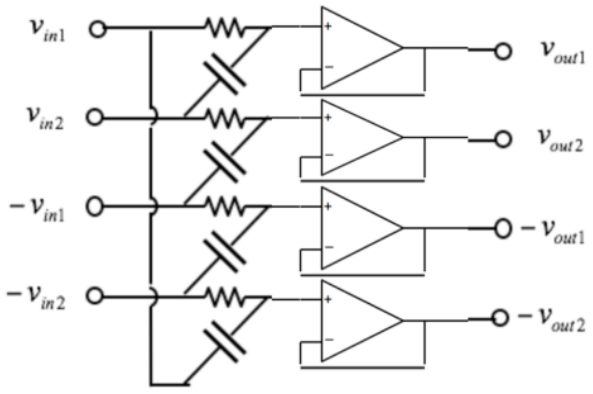

Figure 8. Directly buffered Gingell topology

The topology in Figure 8 simplifies by sacrificing the fully differential nature of the structure. The outputs V_{out1} and V_{out2} require the inputs V_{in1}, Vin2, and $-V_{in1}$. Instead of accepting three inputs, a unity gain inverting stage tied to V_{in1}; locally generating $-V_{in1}$. Figure 9 depicts the reduced Gingell topology.

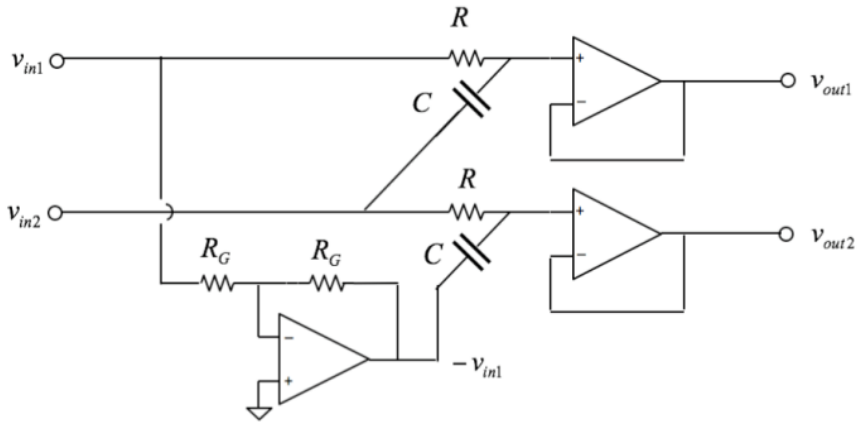

Figure 9. Simplified, Buffered, Gingell topology (2-input)

The network in Figure 9 requires three active components (op-amps) and simplifies the original Gingell topology (Figure 7). The objective of this thesis reduces the number of active components while maintaining the same transfer function from equations 1.17 and 1.18. Chapter 3 derives an active Gingell topology.

2. LITERATURE REVIEW

2.1. Topologies for Use in Image Reject Receivers

"Complex Low-Pass Filters" presents a method of reducing the imbalance of the I and Q paths in a zero-if transceiver [4]. This paper provides analytical and numerical analysis of the complex low-pass filter developed by Kiss, Prodanov, and Glas.

[5] illustrates common image-reject architectures and focuses on complex polyphase filters. The analysis of polyphase responses relies on vector analysis. This paper designs a single stage polyphase filter and relates the design to a cascade.

2.2. Topologies Used/Developed for Phase Splitters (In SSB Transmission)

Sidney Darlington's paper explores how to approximate a constant phase difference over a given frequency range and how to design a network capable of producing that approximation [6]. The Hartley single sideband modulator uses this topology. The method discussed in [6] outlines the construction of constant resistance phase-shifting networks connected in parallel.

Saraga uses phase splitting networks for SSB transmission in [7]. This paper explores phase splitting networks and gives a general design procedure. The paper presents a basic phase splitting network and gives design approximations to create a wide band phase splitting network.

Howard's 1955 paper "A constant phase-difference network and its applications to a filter for an amateur-type transmitter" demonstrates another RC-CR topology. This paper explores the design and implementation of a passive all-pass filter that maintains a constant phase difference on the outputs [8].

Bedrosian's 1960 paper, "Normalized Design of 90° Phase-Difference Networks" presents another implementation of a passive all-pass network that produces two outputs 90-degreess out of phase with each other over a design bandwidth [9]. This paper attempts to simplify the computational complexity by providing normalized tables, used to design a network that operates over a designed frequency band.

The Gingell topology introduced in Figure 7 synthesizes a 90-degree phase shift between the two outputs [1]. To illustrate this, set the input to the network to:

$$V_{in1}(t) = \frac{1}{2}\cos(\omega * t) + \frac{1}{2}\cos(\omega * t) = \cos(\omega * t) \tag{1.33}$$

$$V_{in2}(t) = \frac{1}{2}\sin(\omega * t) + \left(-\frac{1}{2}\sin(\omega * t)\right) = 0 \tag{1.34}$$

The output is calculated as the sum of the response to each input sequence (positive and negative).

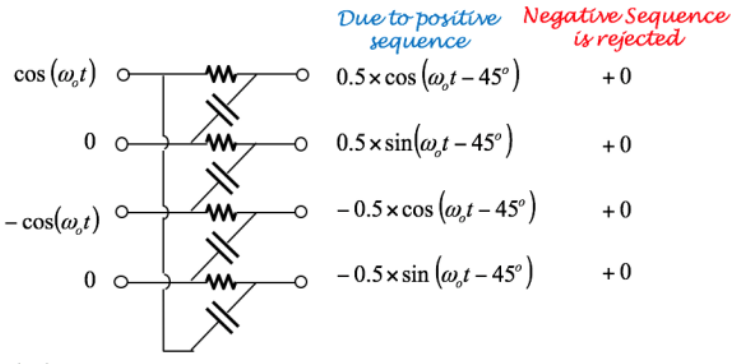

Figure 10. Demonstration of the phase-splitting properties of the Gingell topology

Figure 10 shows that when the input to Gingell network is $(\cos(\omega * t), 0)$ the outputs have the same magnitude and a 90-degree phase shift relative to each other.

2.3. Passive V.S. Active Topologies

[1], [6], [7], [8], and [9] present passive networks that synthesize a phase splitting network between outputs of the system.

In the 2006 paper "An AF All pass Quadrature Networks Practical Approach old Technique Revised" by Siniša, presents an active network that maintains a phase difference between the two output signals [10].

[11] explores an active wideband 90-degree phase splitting network that attempts to reduce the number of different components used.

These sources show that generating quadrature outputs has been a topic of extensive research for the last 65 years.

[12] derives an active RC polyphase filter that requires three operational amplifiers. This topology implements a single pole and an optional zero. This active topology creates arbitrary polyphase transfer functions.

2.4. Impact of Component Mismatches

[8] discusses the importance of component matching in the construction of phase splitting networks.

Siniša presents Monte Carlo analysis to show the influences of component tolerances on the topology [10].

[13] presents another design and analysis of 90-degree phase splitting networks. This work investigates how component variations impact network design. Two passive realizations of phase splitting networks are presented to illustrates the effect of component tolerances.

Hutchins explores the implementation of wideband 90-degree phase splitters without using a wide spread of capacitor values [11]. Selectively grouping poles reduces capacitor spread. Poles are grouped highest and lowest, second highest and second lowest, and so on.

2.5. Other Uses of Hilbert Pairs

[14] details an application of the Hilbert Transform. This tutorial uses the Hilbert Transform in linear and nonlinear vibration analysis. This work discusses realizing the Hilbert Transform in digital signal processing and how to apply the Hilbert Transform to time varying signals. This paper shows phase splitter outputs form a Hilbert Pair.

[15] presents an overview of the Hilbert Transform and then discusses applications of the transform in Signal processing and system identification. In Signal processing the discrete time Hilbert Transform needs to be defined and used to sample bandpass signals. The Hilbert Transform relates the real and imaginary part of the transfer function of a linear time-invariant system.

[16] shows how the Hilbert Transform calculates the analytic signal from an EEG measurement. This article illustrates how time-varying state variables derive from EEG measurements to evaluate cortical states.

[17] presents the topic of the Hilbert Transform and directly applies it to signal processing. The application details using the Hilbert Transform to create amplitude modulated SSB signals.

3. NON-INVERTING TOPOLOGY

3.1. Derivation

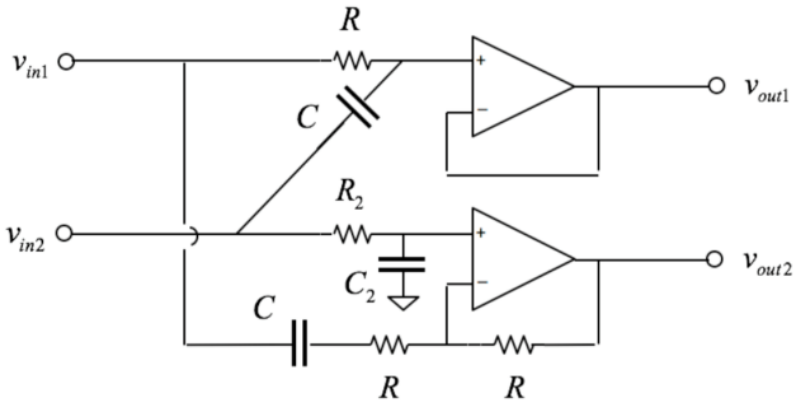

Figure 11. Two-op-amp architecture with sequence asymmetric properties identical to those of Gingell's RC network

Figure 11 shows a 2-input/2-output complex filter that uses two op-amps. The use of op-amps allows this circuit to drive loads without impacting the transfer function. This section derives the transfer function of the network by examining each op-amp individually. The top op-amp creates an active RC low-pass/high-pass filter (Figure 12) and the lower op-amp creates a low-pass response with respect to the first input and a high-pass response with respect to the second input (Figure 13). This topology further reduces of the network shown in Figure 9. Appendix C derives the entire transfer function for each output of Figure 11.

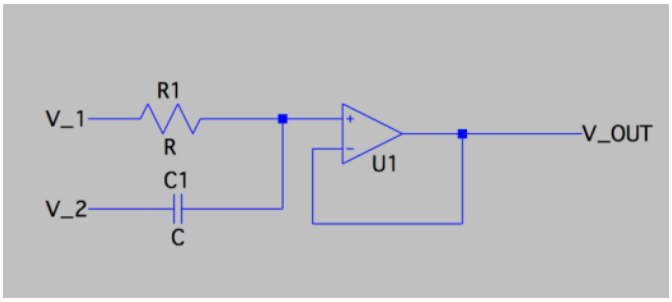

Figure 12. Dual-input LP/HP non-inverting stage

V_{OUT}:

$$V_{OUT} = \frac{1}{1 + s * C * R} * V_1 + \frac{s * C * R}{1 + s * C * R} * V_2 \tag{3.1}$$

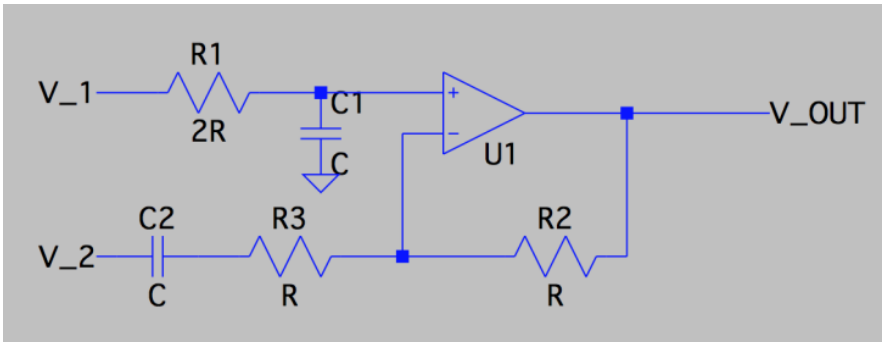

Figure 13. 2-input topology realizes LP TF with respect to v1 and inverting HP with respect to v2

V_{OUT}:

$$V_{OUT} = -\frac{s * C * R}{1 + s * C * R} * V_1 + \frac{1}{1 + s * C * R_2} * \frac{s * 2 * C * R + 1}{s * C * R + 1} * V_2 \tag{3.2}$$

The circuits shown in Figure 12 and Figure 13 combine to produce the complex filter of Figure 11. This circuit takes two inputs and produces two different outputs.

Equations (3.3) and (3.4) summarize the transfer function of the complex filter topology shown in Figure 11:

$$V_{OUT1} = \frac{1}{1 + s * C * R} * V_{in1} + \frac{s * C * R}{1 + s * C * R} * V_{in2} \tag{3.3}$$

$$V_{OUT2} = -\frac{1}{1 + s * C * R} V_{in1} + \frac{1}{1 + s * C * R_2} * \frac{s * 2 * C * R + 1}{s * C * R + 1} V_{n2} \tag{3.4}$$

Setting the value of R_2 to twice the value of R, preserves the system time constant. The equations given in (3.3) and (3.4) reduces to the equations given in (1.17) and (1.18). As a result, the Figure 14 circuit accomplishes the same transfer function given in (1.17) and (1.18) using only two op-amps. This topology is technically a second order filter, but because of the R_2, R relationship (R_2, = 2*R), a pole-zero cancelation occurs. This creates the response shown in Figure 6,c.

SPICE simulation verifies the functionality of the Figure 14 circuit, the input signals tested consist of (cos, -sin), (cos, sin), (cos, cos); corresponding to Figure 15, Figure 16, and Figure 17.

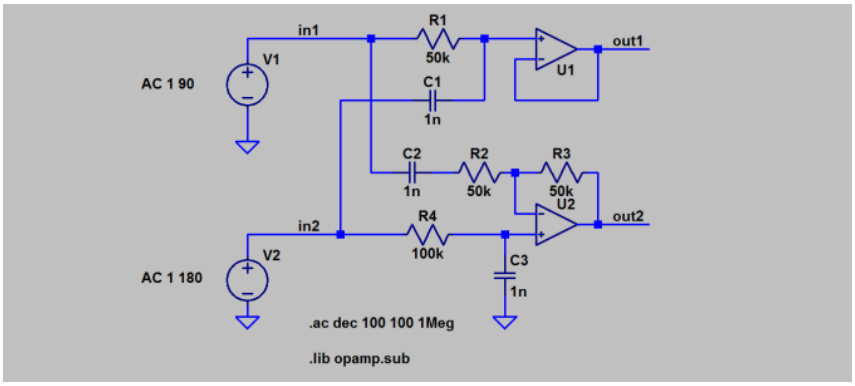

Figure 14. Single-stage complex filter with characteristic frequency (notch) location of 3.183 kHz

The simulated filter has a characteristic frequency of 3.1622 KHz.

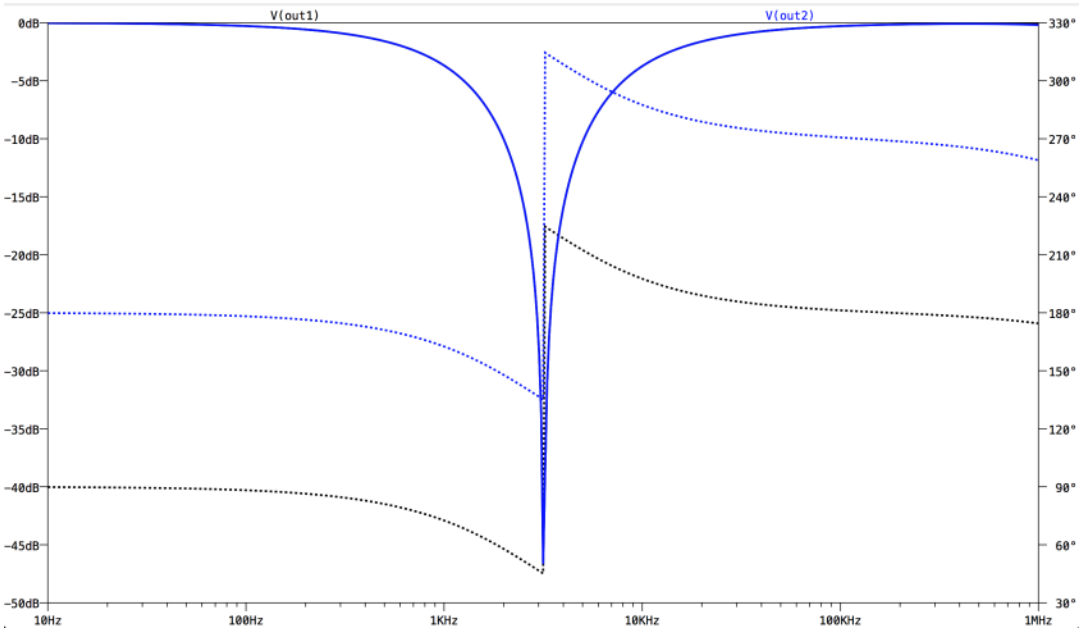

Figure 15. Inputs: COS,-SIN Produces a notch at FC= 3.162kHz Identical Magnitude and Notch

Figure 15 shows that input signals (cos, -sin), a negative 90-degree phase shift between the two inputs, produce a notch response. Both outputs have the same magnitude and notch frequency.

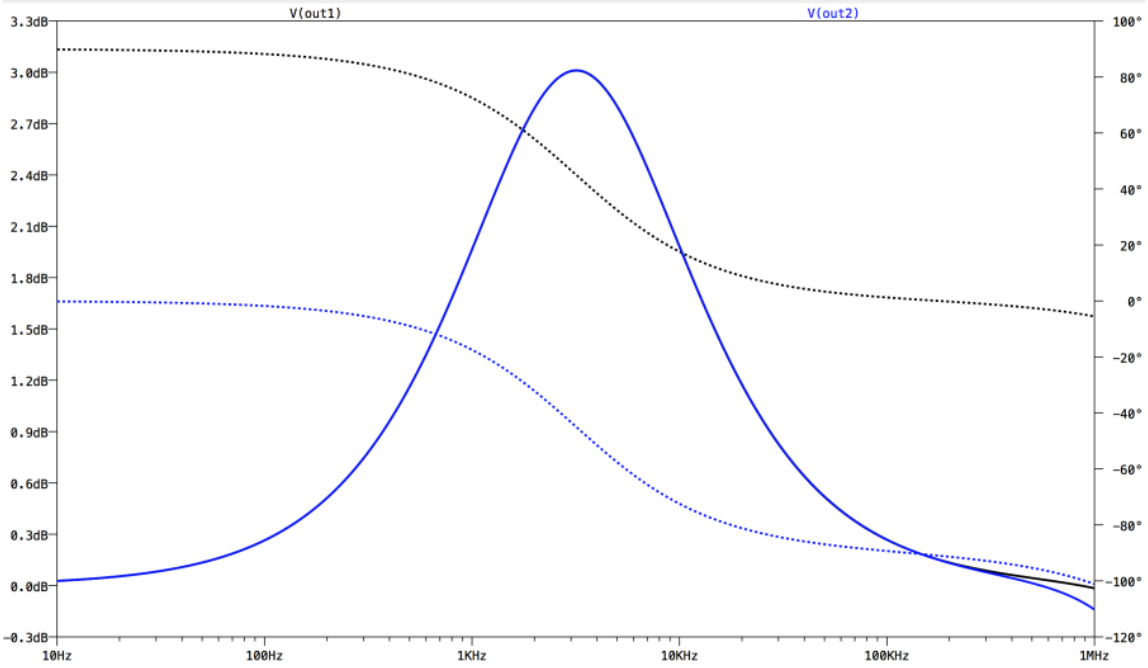

Figure 16. Inputs: COS, SIN Produces a Bandpass at FC= 3.162kHz Identical Magnitude

Figure 16 shows that with input signals (cos, sin), a positive 90-degree phase shift between the two inputs, produce a bandpass response. Both outputs have identical magnitude.

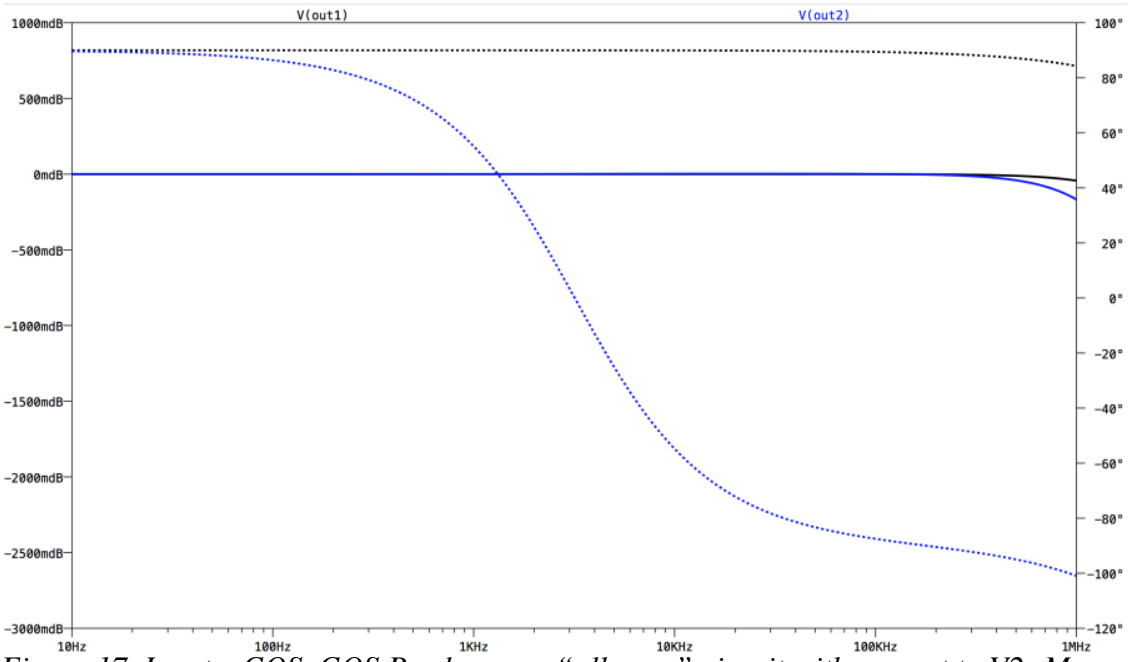

Figure 17. Inputs: COS, COS Produces an "all-pass" circuit with respect to V2; Mag = 1, phase not constant

Inputting signals that have the same phase, such as cosine and cosine produce an all-pass circuit. The magnitude is unaffected, but the phase changes relative to the phase of the input signals. This test also reveals high frequency imperfections related to op-amp finite Gain-BW product.

To investigate the phase splitting capabilities of the topology, ground input 2 and sweep the frequency on input 1. Figure 18 shows the result of phase splitting simulation.

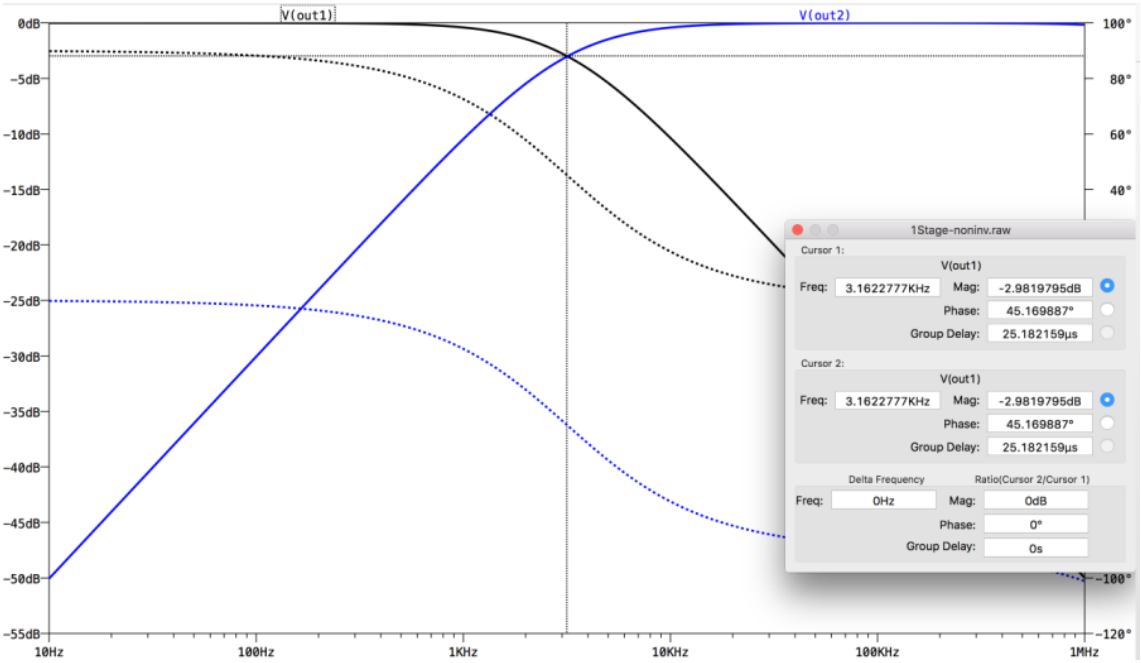

Figure 18. Frequency sweep on one input while input2 = grounded – shows the phase splitting property of the topology

Figure 18 shows that a constant phase difference of 90-degrees exists on the output and magnitude crossover occurs at the characteristic frequency. This simulation shows that phase splitting has a narrow-band response. A broadband response requires a cascade.

3.2. Cascading

The complex filter developed in the Chapter 3.1 creates only one notch and has a passband gain of 3 dB. One of the primary objectives of this thesis designs a filter that has multiple notches; to extend the stopband bandwidth and increase passband gain. Cascading multiple stages of the topology shown in Figure 11 meets this objective. Figure 19 shows the resulting cascade. The outputs of the first filter stage directly connected to the inputs of the second filter stage.

In this example the central frequency of the first stage is 147 Hz. The second stage has a central frequency approximately two times the first stage frequency; 322 Hz. Chapter 4.1 goes into greater detail regarding the importance of the spacing of notch frequencies.

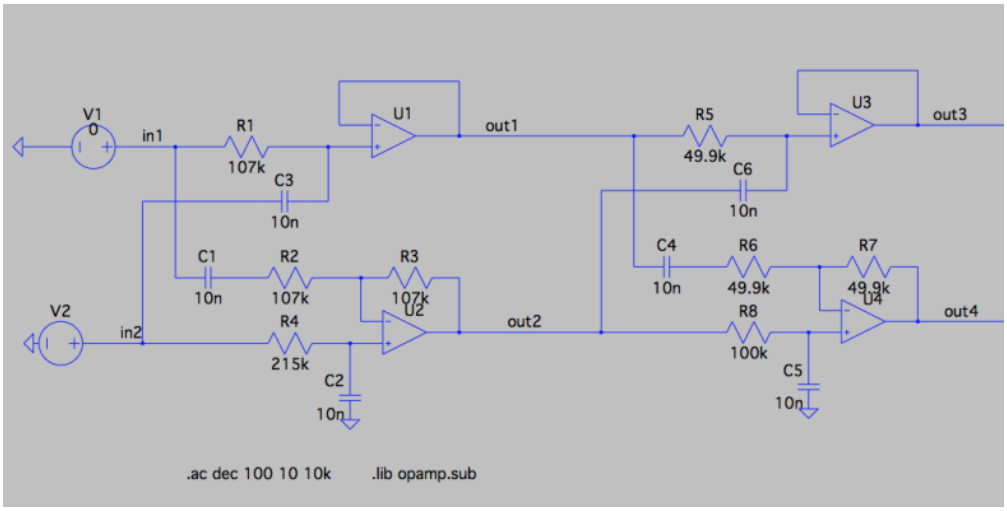

Figure 19. Two stage "Non-Inverting" filter topology

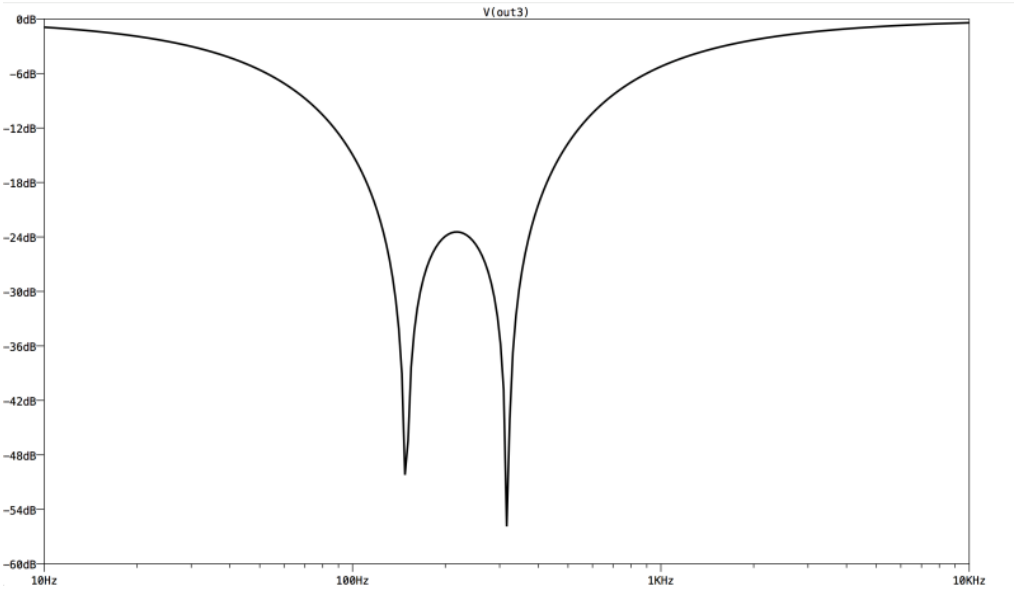

Figure 20. Stopband performance for a two-stage system

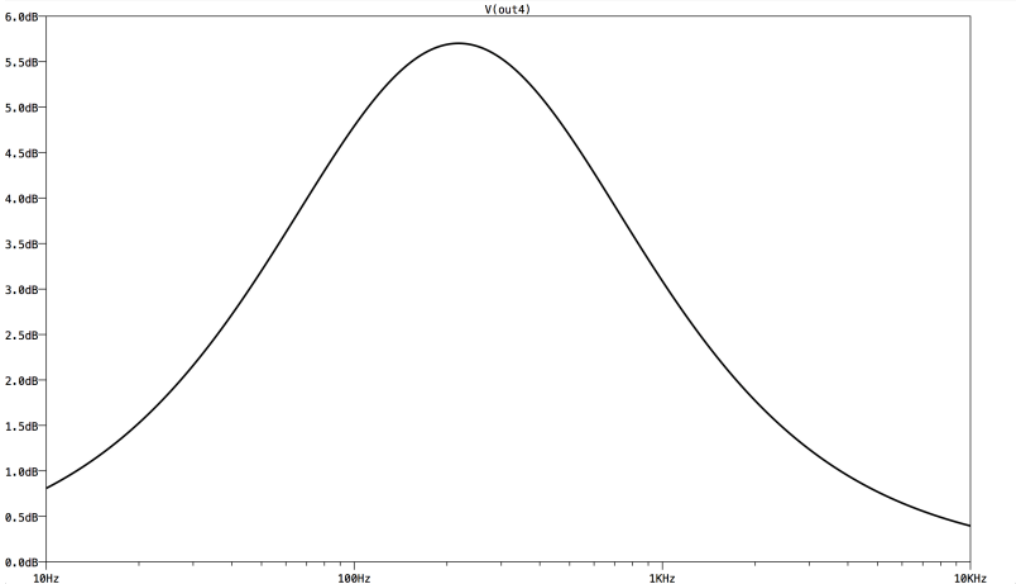

Figure 21. Pass-band response of two-stage system

Figure 20 and Figure 21 show the passband and stopband magnitude response of a two-stage cascade of the complex topology shown in Figure 11. In the stopband, the cascade creates two distinct notches at the filters respective characteristic frequencies. Cascading two notches forms an attenuation "hump" between the first and second notch. The gain of the passband increases in the two-stage implementation over the single stage. The three-stage topology in Figure 22 uses the same central notches from Figure 19 and sets a central frequency to 703 Hz in the third stage.

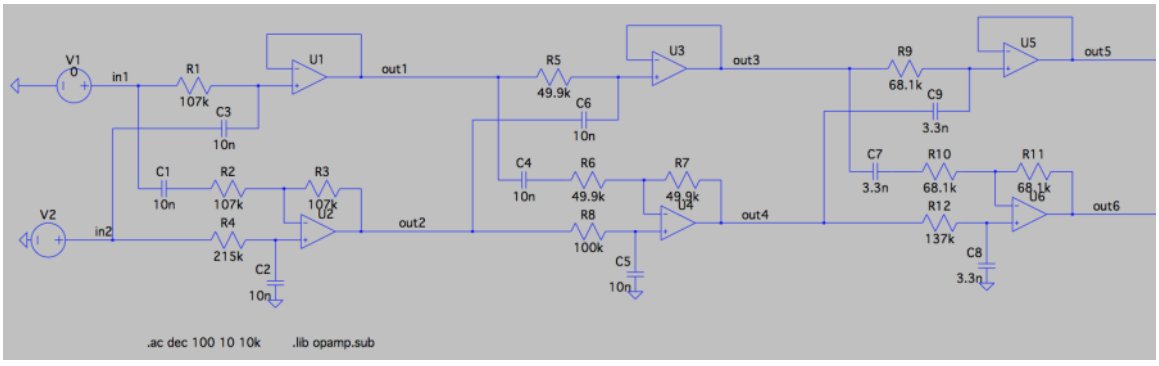

Figure 22. Three stage filter topology

To further illustrate the effect of cascading the “Non-Inverting” topology, Figure 22 shows a three-stage cascade of the Figure 11 topology.

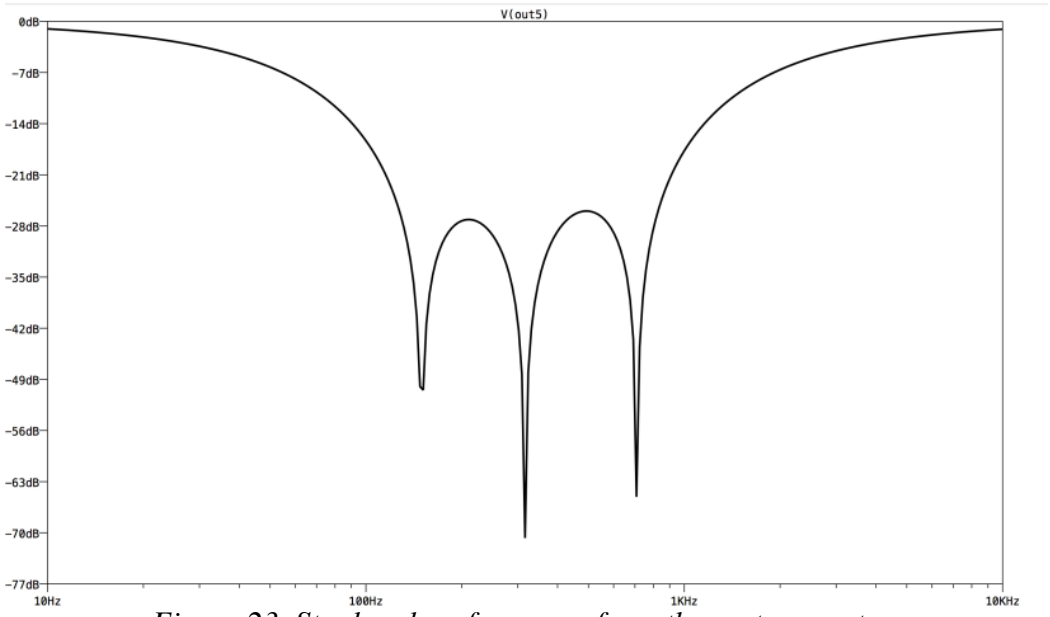

Figure 23. Stopband performance for a three-stage system

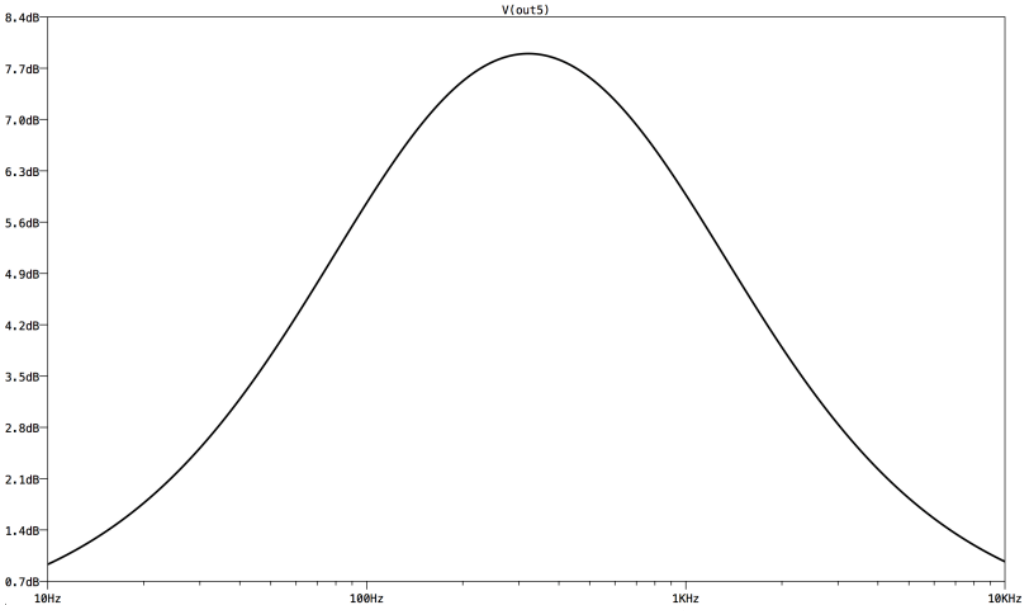

Figure 24. Passband performance for a three-stage system

Figure 23 and Figure 24 show the stopband and passband performance of a three stage-cascade of the complex topology shown in Figure 22. In the stopband, the cascade creates three distinct notches at the filter stage's characteristic frequency. The three-stage cascade forms two attenuation "humps". These "humps" are defined as the relative "attenuation floor" of the complex filter cascade. This floor represents the maximum amount of attenuation that one can expect to see in a cascaded filter topology over the distance from the first characteristic frequency to the last. The gain of the passband continues to increase as stage order increases.

4. MATHEMATICAL DERIVATION OF STOPBAND ATTENUATION

4.1. Definition of Stopband Notch Placement

In a multi-stage cascaded topology, the stopband consists of several notch frequencies. The selected notch frequencies create a symmetric response in a logarithmic frequency plot. Figure 25 demonstrates the stopband symmetry for a multistage configuration. This plot shows how each notch stage contributes to the total response.

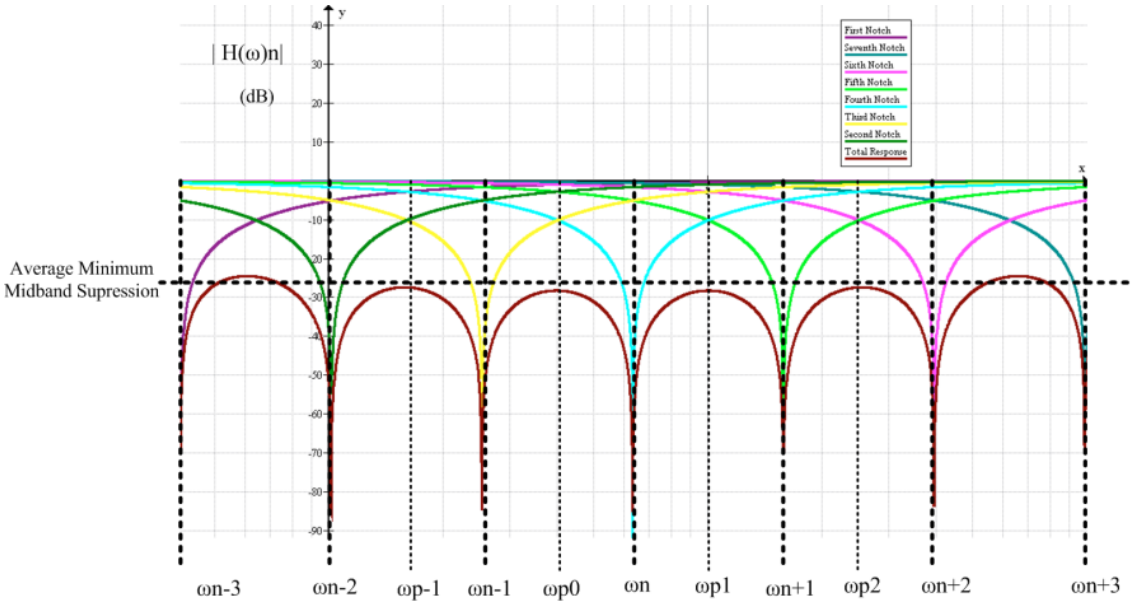

Figure 25. Frequencies of interest for finding average minimum midband suppression

The peaks of these lobes lie in between the successive ω_n locations. The peak frequencies are referred to as $\mathbf{f_{pm}}$ or $\boldsymbol{\omega}_{\mathbf{pm}}$, where "p" stands for "peak" and "m" corresponds to the peak of interest (a number, centered at 0).

Figure 25 shows the midband peaks of interest. f_{pm} refers to the geometric mean of its two neighbor notch frequencies:

$$f_{pm} = \sqrt{f_n \times f_{n-1}} = \frac{\omega_{pm}}{2\pi} \tag{4.1}$$

Where

ω_o = the notch frequency of interest,

ω_n, ω_{n+1}, ω_{n+2} (…) = the notch location due to the stage, and

ω_p= the lobe peak frequency.

k = the ratio between notch frequencies:

$$\frac{f_n}{f_{n-1}} = k \tag{4.2}$$

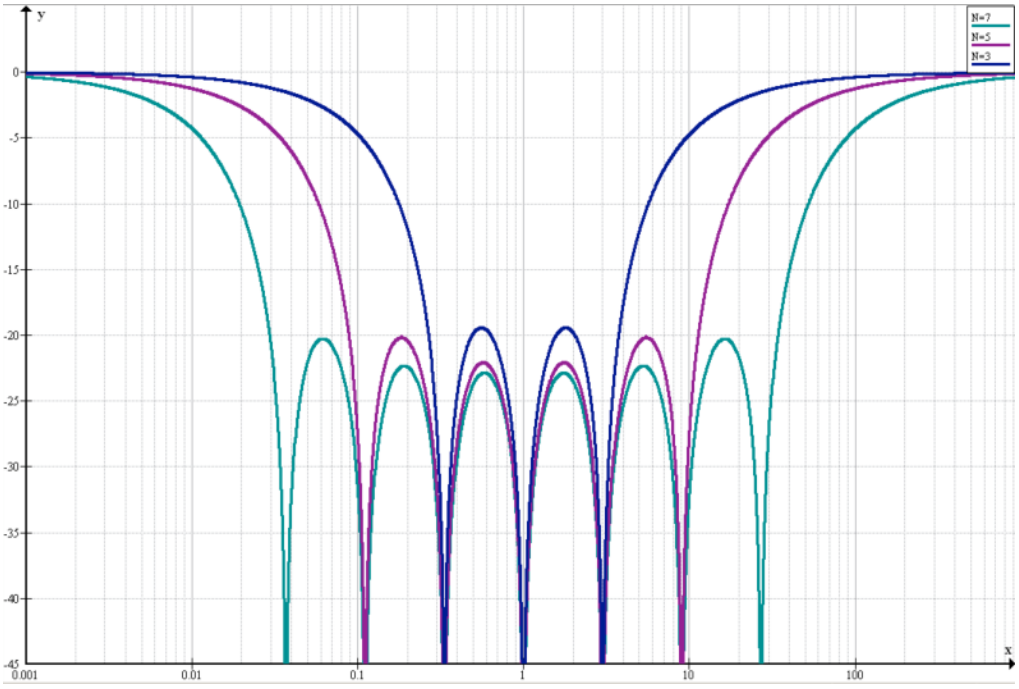

Figure 26. Stop-band plot for N = 3, 5, 7 (normalized frequency)

Figure 26 plots the stopband of an N = 3, 5, and 7 cascade. This figure shows the central frequency corresponds to the middle notch location.

For a system consisting of an odd number of stages, the equidistant notch frequency spacing preserves symmetry with respect to the center frequency (f_o). While maintaining a constant ratio, k, between adjacent notch frequencies, the notch locations to the right of the central frequency are expressed as:

$$f_{+1} = kf_o \ , f_{+2} = k^2 f_o, \ldots f_{+n} = k^n f_o \tag{4.3}$$

Where n corresponds to an integer

Represent the frequencies below the central notch as:

$$f_{-1} = f_o/k \ , f_{-2} = f_o/k^2, \ldots f_{-n} = f_o/k^n \tag{4.4}$$

Where n corresponds to an integer

This notation generalizes to:

$$f_i = k^i f_o \text{ , for } i = -\frac{N-1}{2} \ to \ \frac{N-1}{2} \tag{4.5}$$

Where i corresponds to the offset from the center frequency

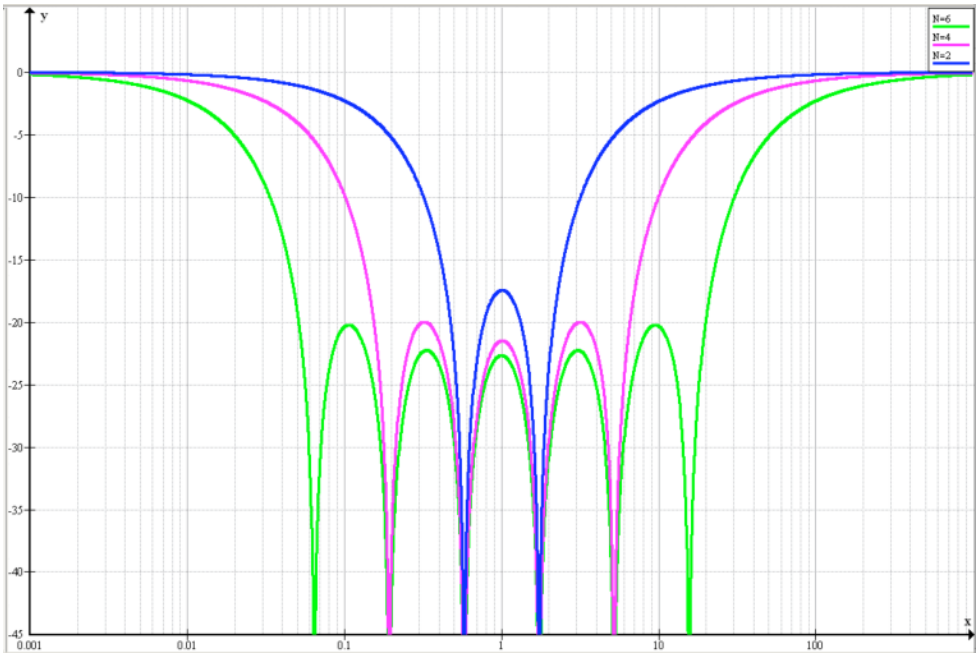

Figure 27. Stop-band plot for N = 2, 4, 6 (normalized frequency) and log scale

Figure 27 plots the stopband for N = 2, 4, and 6. Notice, the central frequency no longer corresponds to a notch frequency. With an even system order, the central frequency corresponds to the peak of the middle attenuation lobe.

For an even number of stages, preservation of symmetry relative to f_o also requires a constant *k*-ratio. However, there is no notch at f_o. When viewed on a normalized logarithmic frequency scale, the notches appear with a $\sqrt{k} * \frac{k}{2}$ (half-distance offset) from f_o. Using the same notation as the odd order network for frequencies above the central frequency:

$$f_{+1/2} = k^{1/2} f_o \ , f_{+3/2} = k^{3/2} f_o, \dots f_{+n/2} = k^{n/2} f_o \qquad (4.6)$$

where n corresponds to an integer

and for the frequencies below the central frequencies:

$$f_{-1/2} = k^{-1/2} f_o,\ f_{-3/2} = k^{-3/2} f_o, \ldots f_{-n/2} = k^{-n/2} f_o, \tag{4.7}$$

where n corresponds to an integer

This notation generalizes to:

$$f_i = k^{i/2} f_o \text{ , for } i = -\frac{N-1}{2}\ to\ \frac{N-1}{2} \tag{4.8}$$

where i corresponds to the offset from the center frequency

Calculating the attenuation lobe heights in the stopband uses Figure 25. This derivation assumes an infinite number of stages. This assumption allows the selection of the central frequency to be any notch location.

The attenuation at a peak frequency of interest in the midband (ω_{p0}) corresponds to the summation of the attenuation attributed to the superimposed notches at ω_n, for all values of n. Because symmetric attenuation occurs, the contributions due to ω_n, ω_{n+1}, ω_{n+2} contribute individually. Determining the magnitude at ω_n, ω_{n+1}, ω_{n+2} depends upon the transfer function of the system, repeated below:

$$|H(\omega)| = \frac{|\omega RC - 1|}{\sqrt{(\omega RC)^2 + 1}} = \frac{\left|\frac{\omega}{\omega_o} - 1\right|}{\sqrt{\left(\frac{\omega}{\omega_o}\right)^2 + 1}} \tag{4.9}$$

Because of the equidistant spacing of the notches and the fact that the peaks fall exactly equidistant between notches, Equation 4.10 determines the attenuation due to the successive stages.

Table 1. Attenuation at stopband peak locations contributed by a single notch

k	Gain at ω_{p0}	Gain at ω_{p1}	Gain at ω_{p2}
	$20\times\log_{10}\left[\frac{\sqrt{k}-1}{\sqrt{k}+1}\right]$	$20\times\log_{10}\left[\frac{k\sqrt{k}-1}{\sqrt{k^3}+1}\right]$	$20\times\log_{10}\left[\frac{k^2\sqrt{k}-1}{\sqrt{k^5}+1}\right]$

Therefore, the gain at a particular ω_{pm} corresponds to:

$$20\times\log_{10}\left[\frac{k^m\sqrt{k}-1}{\sqrt{k^{1+2\times m}}+1}\right] \tag{4.10}$$

For positive m values

Microsoft Excel calculates ω_{pm} values up to $\omega_{p3,}$ given a k range from 1.3 to 3.

Notice Figure 26 and Figure 27 show non-identical attenuation lobes. In cases where $N \geq 3$, the first and last lobe attenuation is less than the attenuation of middle lobes. For example, when N = 5; the first and fourth lobe have identical attenuations less than the attenuation of the second and third lobe. As a result, two cases are evaluated when estimating stopband lobe height; middle lobe attenuation and edge lobe attenuation.

Table 2 contains the calculated values for attenuation peaks. Because the system has symmetric notches, determining the total suppression for the midband adds the suppression contributed by individual notches going in one direction and multiplying it by two. Finding total attenuation for a peak in the edge region multiplies the closest peak attenuation by two and sums it with the remaining attenuations in one direction.

Table 2. Excel calculations of stopband attenuation

	Gain at ω_{p0}	Gain at ω_{p1}	Gain at ω_{p2}	Gain at ω_{p3}	Total gain for midband	Total attenuation for midband	Total gain for edge	Total attenuation for edge
1.3	-20.683	-11.382	-7.392	-5.067	-89.052	89.052	-65.210	65.210
1.4	-18.542	-9.388	-5.641	-3.591	-74.328	74.328	-55.707	55.707
1.5	-16.945	-7.954	-4.452	-2.652	-64.010	64.010	-48.950	48.950
1.6	-15.687	-6.867	-3.603	-2.021	-56.360	56.360	-43.868	43.868
1.7	-14.660	-6.015	-2.974	-1.578	-50.459	50.459	-39.890	39.890
1.8	-13.800	-5.330	-2.494	-1.258	-45.767	45.767	-36.683	36.683
1.9	-13.064	-4.768	-2.120	-1.019	-41.947	41.947	-34.038	34.038
2	-12.426	-4.300	-1.823	-0.837	-38.776	38.776	-31.815	31.815
2.1	-11.866	-3.905	-1.583	-0.696	-36.103	36.103	-29.917	29.917
2.2	-11.368	-3.568	-1.386	-0.585	-33.817	33.817	-28.276	28.276
2.3	-10.922	-3.277	-1.223	-0.496	-31.839	31.839	-26.842	26.842
2.4	-10.520	-3.024	-1.086	-0.424	-30.112	30.112	-25.576	25.576
2.5	-10.155	-2.802	-0.970	-0.366	-28.589	28.589	-24.449	24.449
2.6	-9.8215	-2.607	-0.872	-0.317	-27.236	27.236	-23.440	23.440
2.7	-9.5155	-2.433	-0.787	-0.276	-26.026	26.026	-22.529	22.529
2.8	-9.233	-2.278	-0.713	-0.242	-24.937	24.937	-21.702	21.702
2.9	-8.972	-2.139	-0.649	-0.214	-23.952	23.952	-20.948	20.948
3	-8.7297	-2.014	-0.593	-0.189	-23.055	23.055	-20.257	20.257

Based on the values calculated in Excel, total "middle lobe" attenuation was plotted against the given k value (Figure 28). Fitting the data with a power-law trend line gives Equation 4.11:

$$middle\ lobe\ attenuation = 119.69k^{-1.556} \tag{4.11}$$

Equation 4.11 allows a designer to determine and calculate the approximate attenuation of the middle lobes in the stopband of a cascaded topology given a k value (4.2) that ranges from 1.4 to 3. The attenuation given by Equation 4.11 does not yield an exact result due to the simplifying assumptions made in creating Table 2.

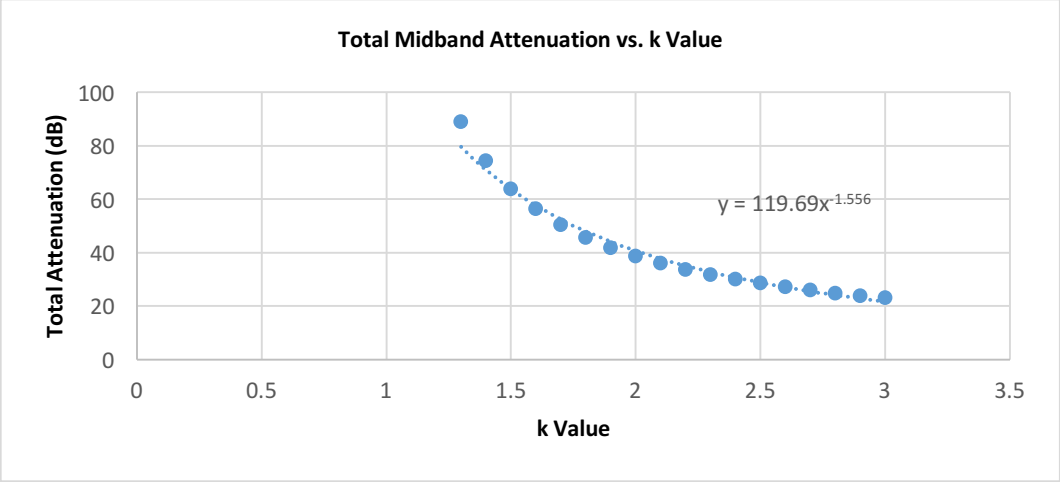

Figure 28. Graph of total attenuation (middle lobe) versus k

The data obtained in Table 2 graph of the total attenuation in the edge lobes versus the given k value (Figure 29). Fitting the data with a power trend line gives Equation 4.12:

$$edge\ lobe\ attenuation = 84.131 * k^{-1.344} \tag{4.12}$$

Similar to Equation 4.11, Equation 4.12 gives an approximation of edge lobe attenuation. The trend line provides an accurate approximation when k ranges from 1.4 to 3.

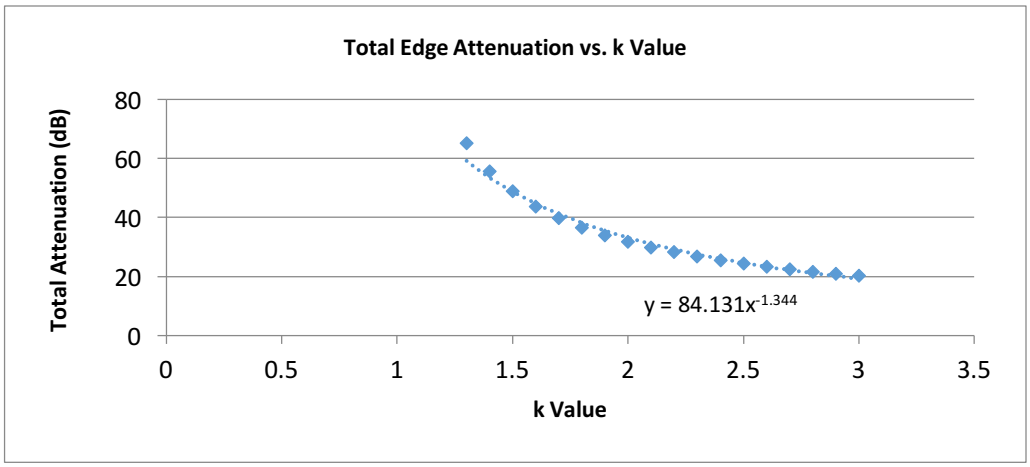

Figure 29. Graph of total attenuation (edge lobe) versus k

4.2. Definition of Stopband Bandwidth

In the case of positive frequency, bandwidth measurements require little attention. Since the filter exhibits a band-pass response, locate the central peak and measure 3dB down on either side to determine bandwidth. Determining the stopband bandwidth presents much more of a challenge. Using a similar approach to the passband case in the stopband involves measuring 3dB down from 0dB on either end of the stopband. This metric yields a measured stopband much larger than the targeted passband bandwidth. Another approach would first locate the "attenuation floor" in the stopband. Then measure at which point the first and last time the response crosses this level; illustrated in Figure 30. Bandwidth becomes dependent on the "attenuation floor" of the cascaded response. This yields a better representation of stopband than simply using -3dB points, however it presents a mathematically challenging measurement model.

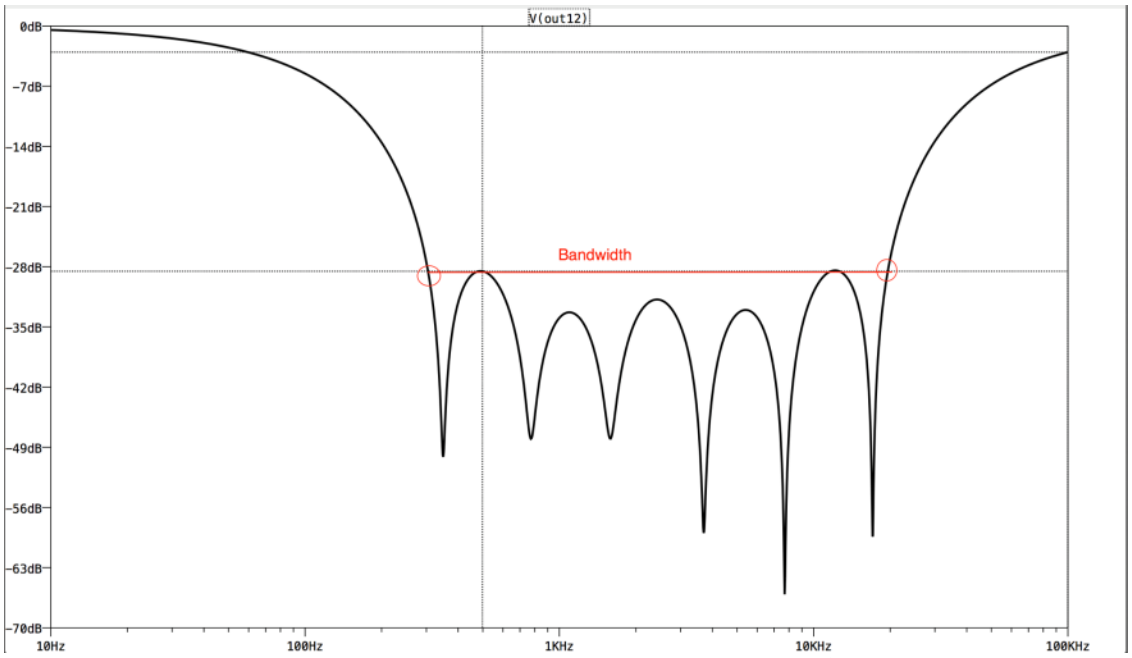

Figure 30. "Attenuation floor" bandwidth

The simplest measurement definition of stop-band bandwidth is the distance between the first and last notches. This measurement captures the performance of the design because specific notch placement allows the designer to use the distance between the first and last notches to find system bandwidth. This bandwidth decides the stage order. Figure 31 presents an example of this bandwidth measurement. Equation 4.13 determines stopband bandwidth:

$$\frac{BW}{f_o} \equiv k^{\frac{N-1}{2}} - k^{-\frac{N-1}{2}} \tag{4.13}$$

Equation 4.13 depends on the notch placement relevant to the central frequency and applies to both even and odd stage configurations. A notch-to-notch bandwidth simplifies measurements, and relates to the number of stages (N) and frequency spacing (k) to system bandwidth. This "conservative" measurement provides the designer with a worst-case measurement of bandwidth.

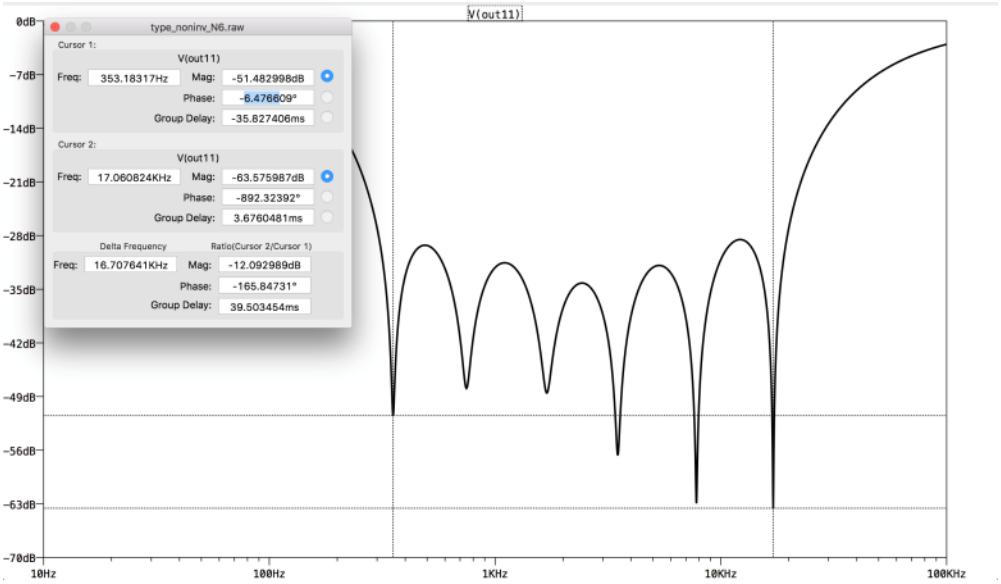

Figure 31. Notch-to-notch Bandwidth

4.3. Design Example

4.3.1. Calculation and Simulation

This section demonstrates the utility of the topology shown in Figure 11. A five-stage network has a central frequency of 703 Hz and a minimum of 30 dB of attenuation in the stopband. This central frequency corresponds to the peak human speech frequency sensitivity range [18].

Equation 4.12 determines frequency spacing, k, from its relationship to attenuation.

$$30dB = 84.131 * k^{-1.344}, k = 2.15 \tag{4.14}$$

Equation 4.5 yields the characteristic frequencies for each stage

$$f_i = 2.15^i * 703 \text{ , for } i = -\frac{5-1}{2} \; to \; \frac{5-1}{2} \tag{4.15}$$

Table 3. Corner frequencies selected in design example

Corner Frequencies	147 Hz	322 Hz	703 Hz = f_o	1534 Hz	3344 Hz

Using [19] determines the exact passband gain:

$$3 + 40 \sum_{l=1}^{\frac{5-1}{2}} \log_{10} \frac{2.15^l + 1}{\sqrt{2.15^{2l} + 1}} = 10.851\ dB \tag{4.16}$$

Using the characteristic frequencies in Table 3, a five-stage cascade of the filter in Figure 11 was created. Resistor and capacitors set the desired characteristic frequencies. Table 4 shows ideal component values.

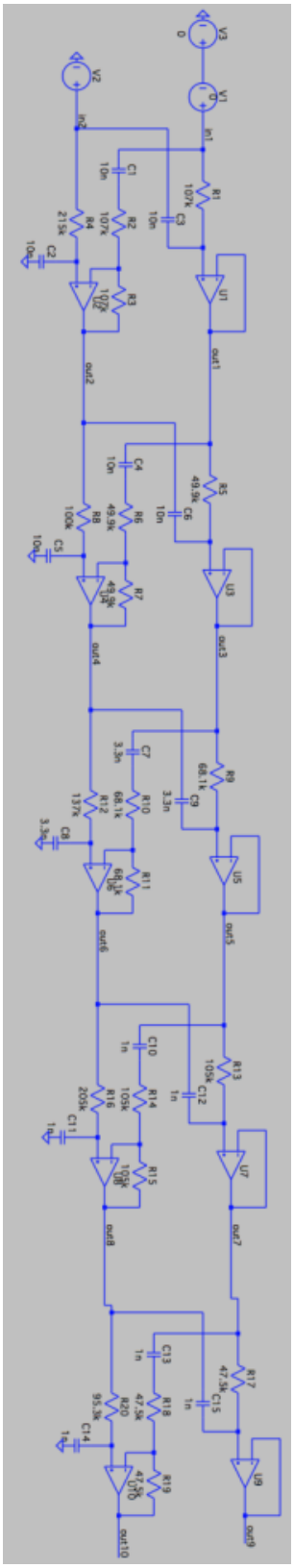

Figure 32. Non-Inverting topology, 5 stages cascaded, ideal component values

LTSpice simulation verifies the operation of Figure 32 circuit. Figure 33 presents the results of simulation using Ideal components, given in Table 4.

Table 4. Ideal resistor values for each stage of non-inverting topology

Resistor	**Stage 1**	**Stage 2**	**Stage 3**	**Stage 4**	**Stage 5**
R1	108.269k	49.4k	68.604k	103.752k	47.5231k
R2	216.53k	98.85k	137.208k	207.503k	95.0462k

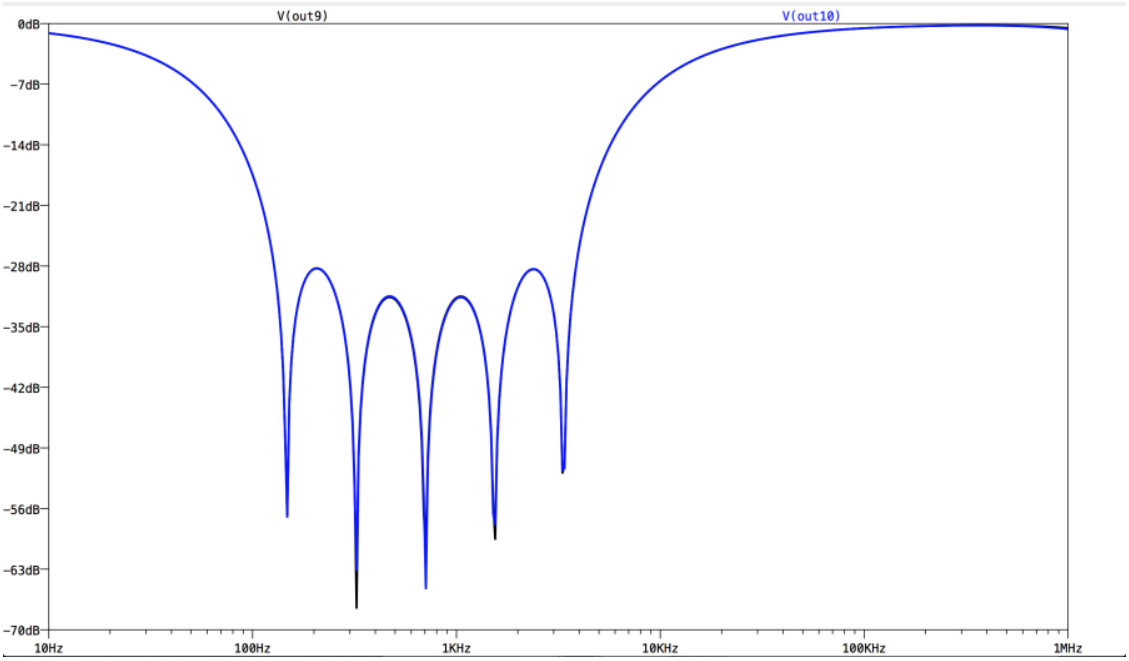

Figure 33. Non-inverting topology outputs for ideal component values

Figure 33 shows the two outputs of the circuit with inputs of V1 = cosine and V2 = –sine. Both outputs exhibit the same magnitude response (two curves plotted but only one seen as outputs overlap). "Attenuation floor" = -28.33 dB using ideal components.

4.3.2. Component Selection For Design Implementation

One of the key challenges in implementing the design using "real world" components requires that $R_2 = 2*R_1$. The following discussion compares two methods of maintaining the R_2/R_1 relationship. The first rounds all ideal values to the nearest 1% component, and the second creates the R_2 resistor by using a series combination of two R_1 resistors.

To perform a preliminary investigation on component tolerance variations, standard 1% tolerance values replace the ideal values found in Table 4. These new values are shown in Table 5. Figure 34 shows the outputs of the circuit with standard values.

Table 5. Standard 1%(E96) values for non-inverting topology

Resistor	**Stage 1**	**Stage 2**	**Stage 3**	**Stage 4**	**Stage 5**
R1	107k	49.9k	68.1k	105k	47.5k
22	215k	100k	137k	205k	95.3k

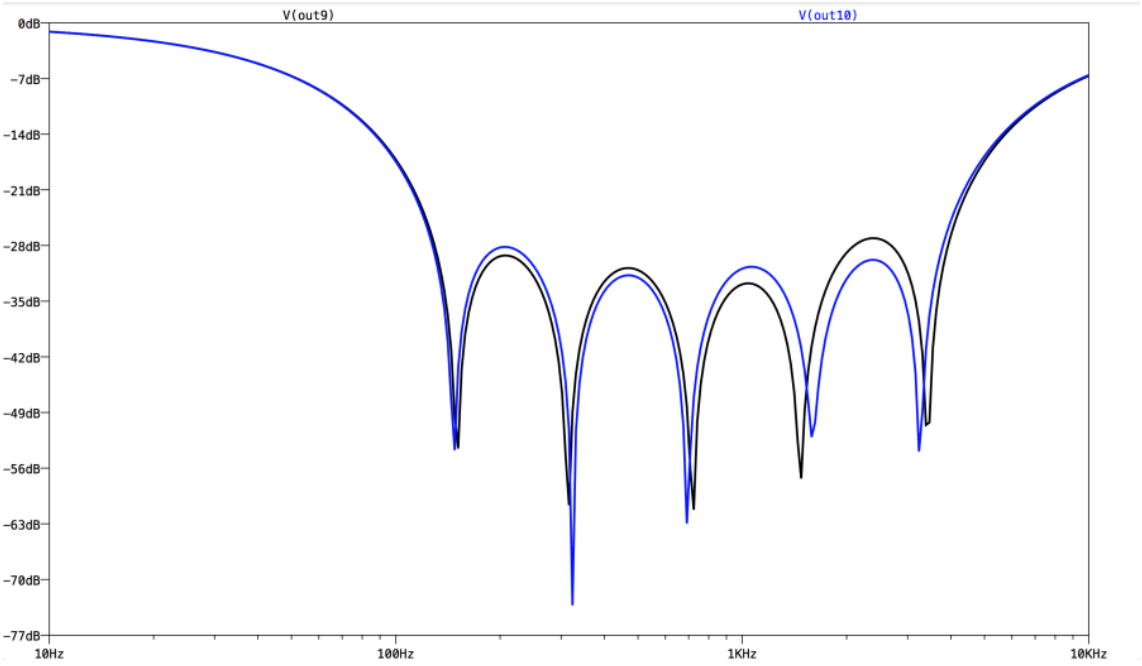

Figure 34. Non-inverting topology outputs for standard 1% tolerance component values

Figure 34 show that rounding component values changes the stopband performance. The notches in outputs 9 and 10 no longer match exactly and the attenuation between the two outputs differs. Out9 has an “attenuation floor” of 27.080 dB and out10 has an “attenuation floor” of 28.179 dB. Out10 compares favorably with the ideal component simulation where “attenuation floor” = -28.33 dB, while out9 has 1.25 dB less attenuation than the ideal simulation.

Table 6 shows the selected standard one percent component values where the R2 resistor corresponds to a series combination of two R1 resistors. Figure 35 shows the output of the circuit with those values.

Table 6. Standard 1% values for non-inverting topology, R2 as series combination of R1

Resistor	**Stage 1**	**Stage 2**	**Stage 3**	**Stage 4**	**Stage 5**
R1	107k	49.9k	68.1k	105k	47.5k
R2	214k	99.8k	136.2k	210k	95k

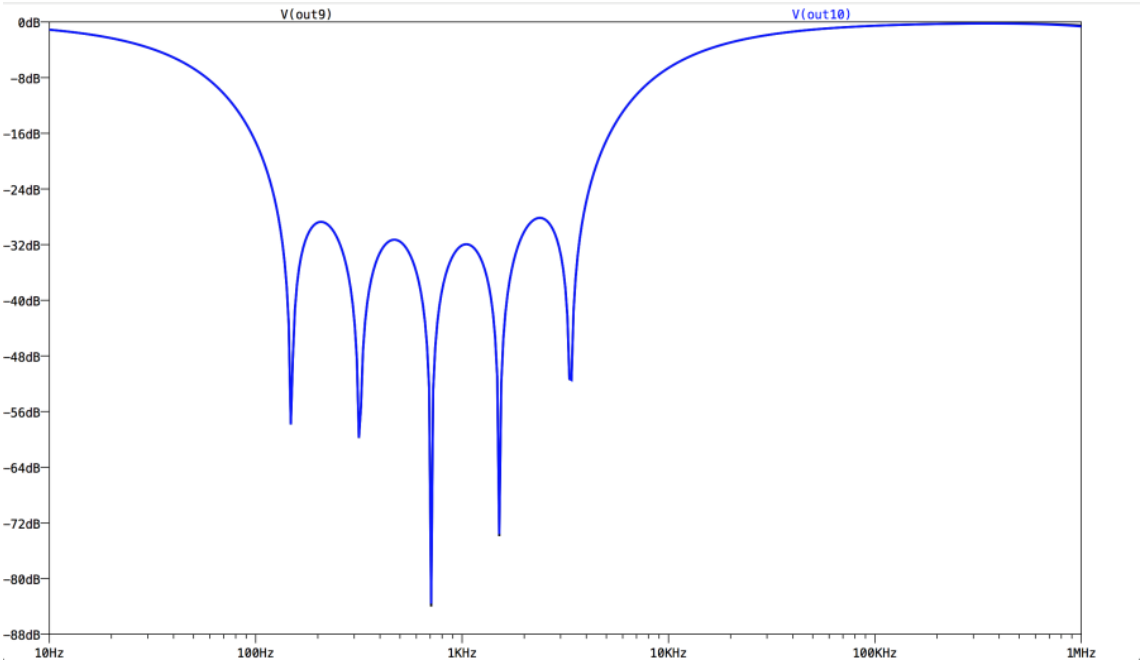

Figure 35. Non-inverting topology outputs for standard 1% tolerance component values, R2 as series combination of R1

By switching to R2 = 2*R1 values instead of using rounded 1% components, the notch frequencies and attenuation of the peaks match for the two outputs. This choice of values provides three advantages: precise notch frequency locations, output magnitude matching, and fewer different-value resistors for construction.

Both outputs exhibit the same “attenuation floor”; 28.157 dB. This compares favorably with the ideal component simulation.

4.3.3. Summary of Simulation Resistor Variations

Table 7 compares the results of notch frequency locations for each stage of the filter constructed in Figure 32 depending on the resistor configuration selection. This table shows that resistor precision does cause the notch location to shift. Chapter 5.3 details the effect of component tolerances. From this table, note that resistor configuration must be taken into account in a precise design, but in most cases any configuration meets design specification within 10 percent of ideal component values.

Table 7. Notch frequencies for different resistor configurations

Configuration:	**Notch 1**	**Notch 2**	**Notch 3**	**Notch 4**	**Notch 5**
Desired Value	147 Hz	322 Hz	703 Hz	1534 Hz	3344 Hz
Non-Inverting, K = 2.1867					
Ideal Component Values	147.428	323.850	706.553	1546	3359
1% Resistor Values Out10	146.095	323.328	694.728	1589	3255
1% Resistor Values Out9	149.948	313.491	720.007	1473	3432
1% Resistor Values In Series	148.004	315.987	706.700	1513	3332

Table 8. "Attenuation floor" lobe heights for different resistor configurations

Configuration:	First Peak	Second Peak	Third Peak	Fourth Peak
Non-Inverting, K=2.1867				
Ideal Component Values	-28.292	-31.494	-31.608	-28.340
1% Resistor Values Out9	-29.253	-30.831	-32.753	-27.080
1% Resistor Values Out10	-28.181	-31.747	-30.675	-29.800
1% Resistor Values In Series	-28.732	-31.303	-31.950	-28.159

Table 8 compares the stopband lobe attenuations created by the five-stage cascade for each simulated resistor configuration. Similarly to the notch locations, resistor configuration does affect attenuation, but all configurations meet an attenuation floor specification within 10 percent.

4.3.4. Prototyping Design Example

This example constructs the filter using 1% components after verifying that the filter design meets specification in simulation. While the results in Figure 34 show that using standard 1% component values did not perfectly match the ideal component simulation shown in Figure 32, selecting 1% component values reduce complexity in construction of the filter network. Table 9 shows the resistors and capacitors used in prototype testing. Prototyping utilizes the MCP6282 op-amp. The MCP6282's rail-to-rail characteristics and high Gain Bandwidth Product relative to designed characteristic frequencies make it well suited for this application. The Gain Bandwidth Product of the MCP6282 is 5 MHz. This IC has two op-amps per package. Prototyping requires 5 MCP8262 packages.

Table 9. Component values for design example

Stage	**Notch Frequency (Hz)**	**Component Values**	
		Standard 1% Capacitor (nF)	***Standard 1% Resistor (kΩ)***
1	151	10	108
2	326	10	49.9
3	700	3.3	68.1
4	1505	1.0	105
5	3236	1.0	47.5

Figure 36 shows the physical implementation using the components shown in Table 9.

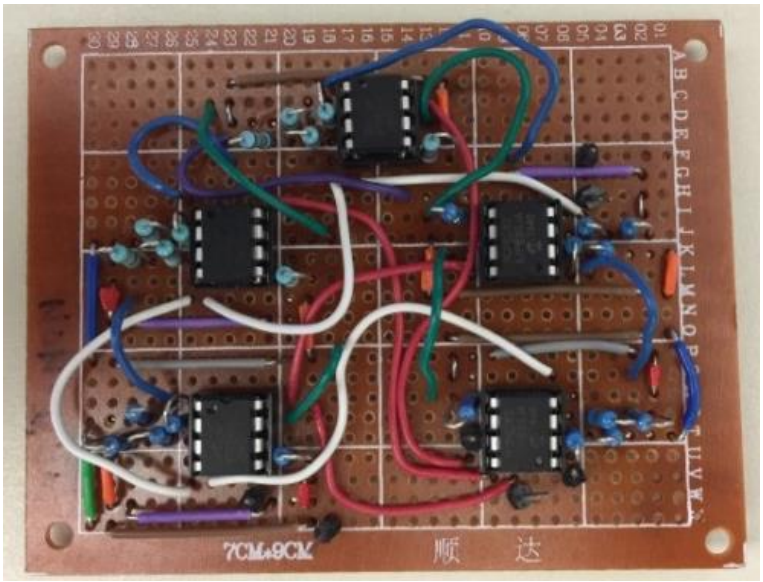

Figure 36. Five-stage active complex filter prototype implemented using five dual op-amp chips on a perforated board

Figure 37 shows the magnitude of response of the circuit under quadrature drive input compared to simulation.

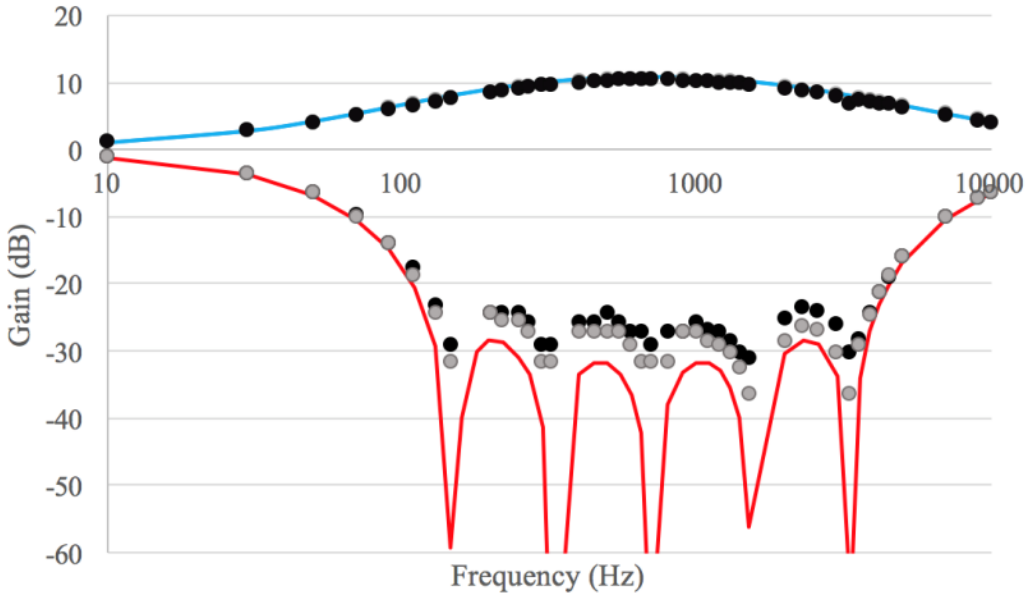

Figure 37. Filter magnitude for the image reject operation

Figure 38 and Figure 39 graph the output over input frequency using a quadrature input.

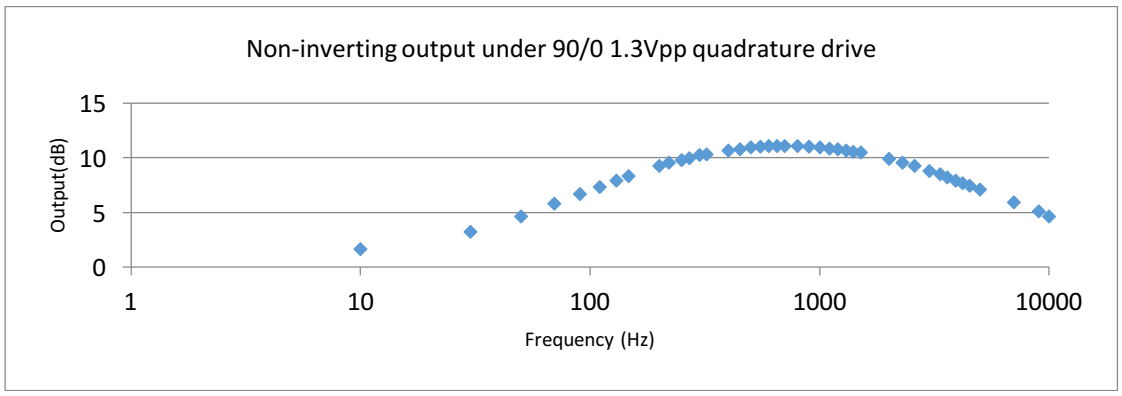

Figure 38. Non-inverting configuration output for 90/0 quadrature

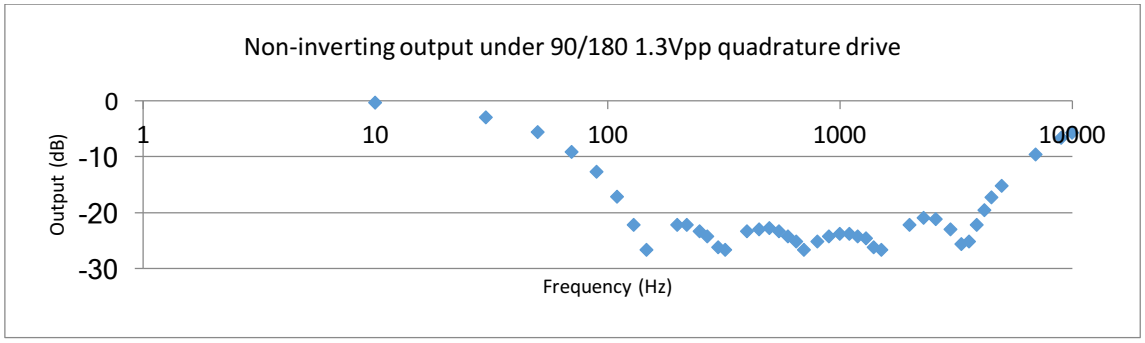

Figure 39. Non-inverting configuration output for 90/180 quadrature

As previously stated, to implement the five-stage cascade, round ideal components to the nearest E96 value. Looking at the difference between out9 and out10 (black and grey dots) in Figure 37 shows similar stopband performance to the LTSpice simulation found in Figure 34. This simulation produces two identical outputs.

Measuring output signals creates errors. At approximately $-30dB$, noise impacts the measured signal. This makes precise magnitude measurements very difficult. Also, the quadrature signal generated may create a parasitic sequence that affects the response of the filter.

Measurements were performed using the RIGOL DG1062Z function generator, the Agilent MSO-X 2012A oscilloscope, and a HP 6235A power supply.

5. MONTE CARLO ANALYSIS

This section investigates the robustness of multi-stage filters implemented with the "Non-Inverting" filter topology discussed in Chapter 3 and the “Inverting” filter topology discussed in Hay [19]. First, an investigation of the level of achieved attenuation between attenuation lobe frequencies in the two topologies determines if one topology has a clear advantage over the other. Next, Monte Carlo analysis determines if filter stage order affects overall system attenuation. In a multi-stage topology where the number of stages, designated as N, creates N! different orderings of the topology. Finally, Monte Carlo analysis investigates the effect of component tolerances on the robustness of the “Non-Inverting” topology.

5.1. Attenuation Estimates

5.1.1. Comparison of Non-Inverting and Inverting Attenuation at Design Frequencies and a Comparison to The “Standard” Gingell Topology

This analysis determines the strengths of each topology. In this simulation k = 2.1867 and utilizes ideal component values. Figure 33 and Figure 40 show the schematic used in Monte Carlo analysis. For both the non-inverting and inverting cases, the edge peaks and middle peaks compare relative to each other to explore how the topology responds to component variation at different frequencies using Monte Carlo analysis.

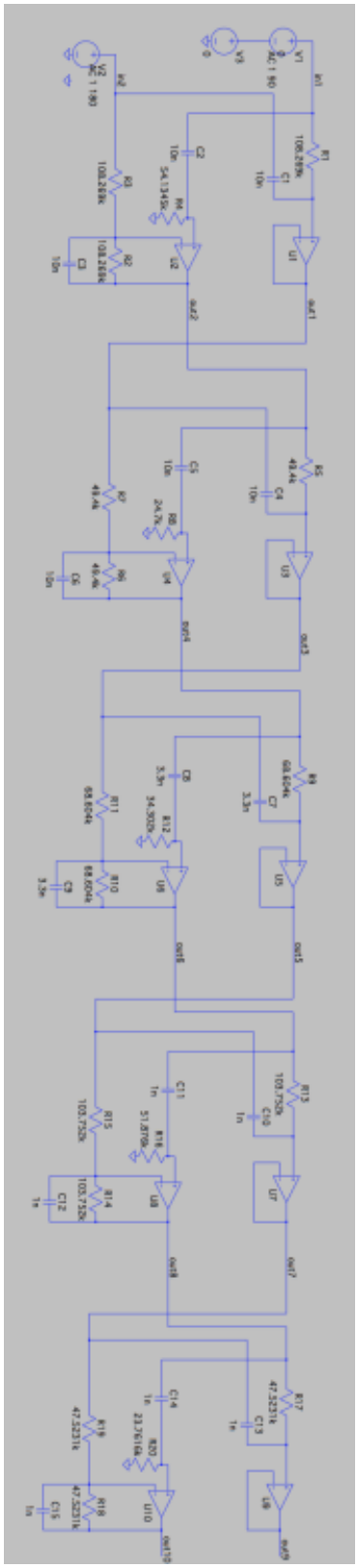

Figure 40. 5-stage filter that uses the "Inverting" topology

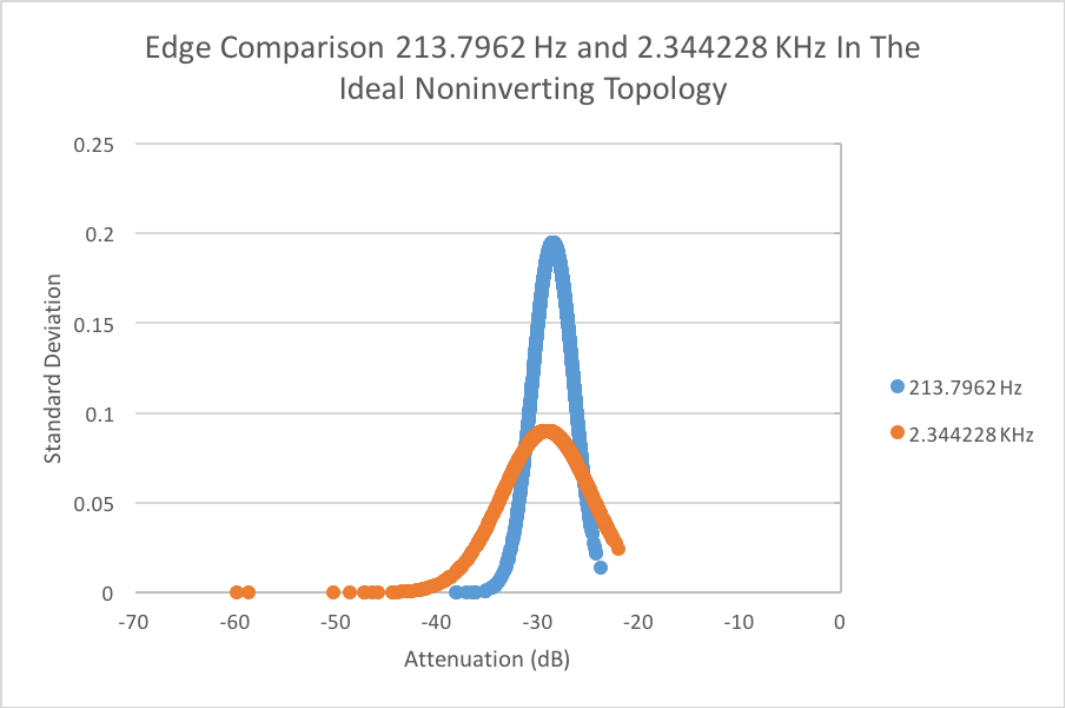

Figure 41. Comparison of edge peaks in a 5-stage filter implemented using Figure 33

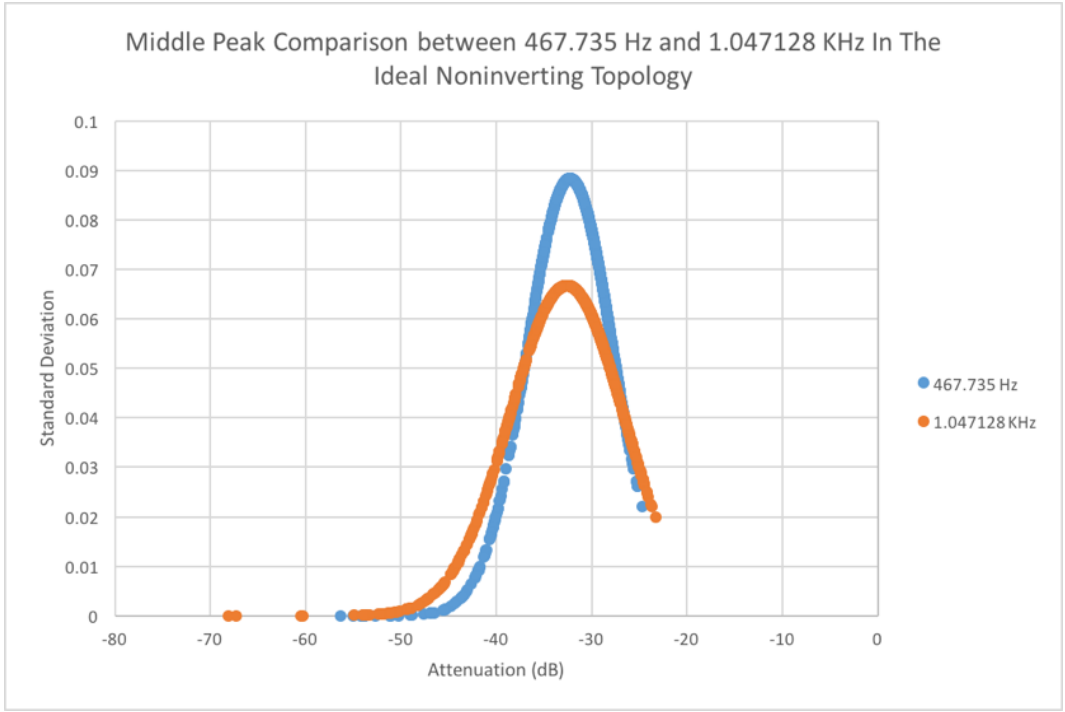

Figure 42. Comparison of middle peaks in a 5-stage filter implemented using Figure 33

Table 10. Comparison of attenuation and standard deviation of peak frequencies in the "Non-Inverting" topology

Peak	Average Attenuation (dB)	Standard Deviation (dB)
Edge Peak 1 (213.796 Hz)	28.555	2.048
Edge Peak 2 (2.344 KHz)	29.175	4.427
Middle Peak 1(467.735Hz)	32.268	4.518
Middle Peak 2(1.047 KHz)	32.598	5.982

Figure 41 compares the two peak edge lobe frequencies and Figure 42 compares to two middle lobes in a Monte Carlo analysis that runs 1000 times. The edge lobe frequencies exhibit more sensitivity to component variation than the middle peaks. At 213.796 Hz the five-stage filter that uses the "Non-Inverting" topology has an average attenuation of 28.555 dB and a standard deviation of 2.048. The other edge frequency, 2.344 KHz, has an average attenuation of 29.175 dB and a standard deviation of 4.427 dB. The trace at 2.344 KHz exhibits greater spread than at 213.796 Hz. As the frequency increases, the spread of the distribution also increases.

The middle lobes have an average attenuation of 32.268 dB at 467.735 Hz and 32.598 dB at 1.947 KHz. The first middle lobe has a standard deviation of 4.518 dB and the second peak has a standard deviation of 5.982 dB. This shows that the topology exhibits less sensitivity to resistor and capacitor tolerances in the middle lobes when compared to the edge lobes. The middle peaks have similar attenuations and standard deviations.

Figure 41 shows that in the five-stage filter using the "Non-Inverting" topology frequency has an impact on how the system responds to resistor and capacitor tolerance variation. The edge lobes exhibit greater variation than the middle lobes relative to each other but the middle lobes both have large standard deviations.

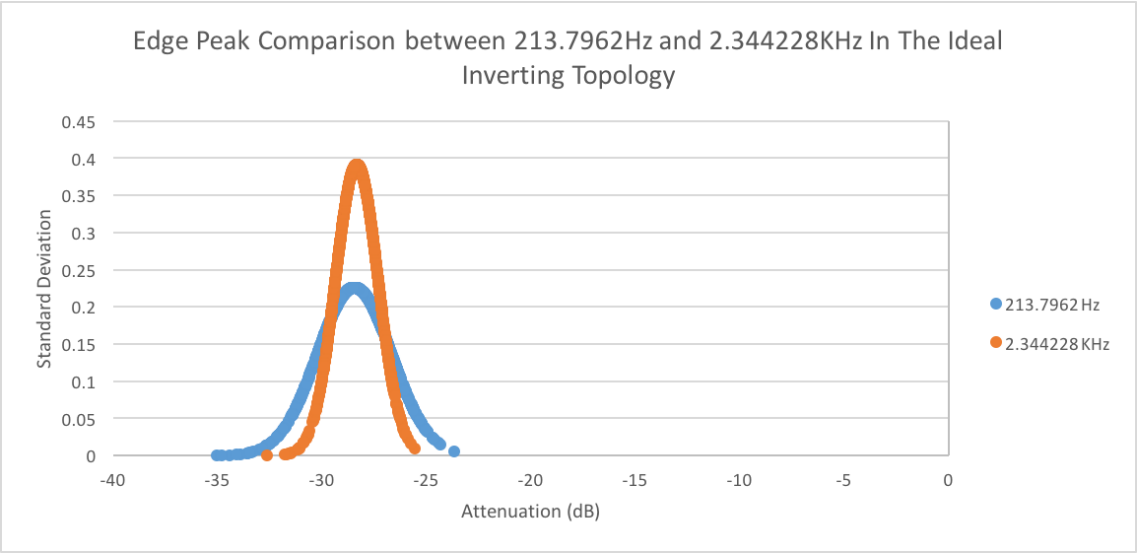

Figure 43. Comparison of edge peaks in a 5-stage filter implemented using Figure 40

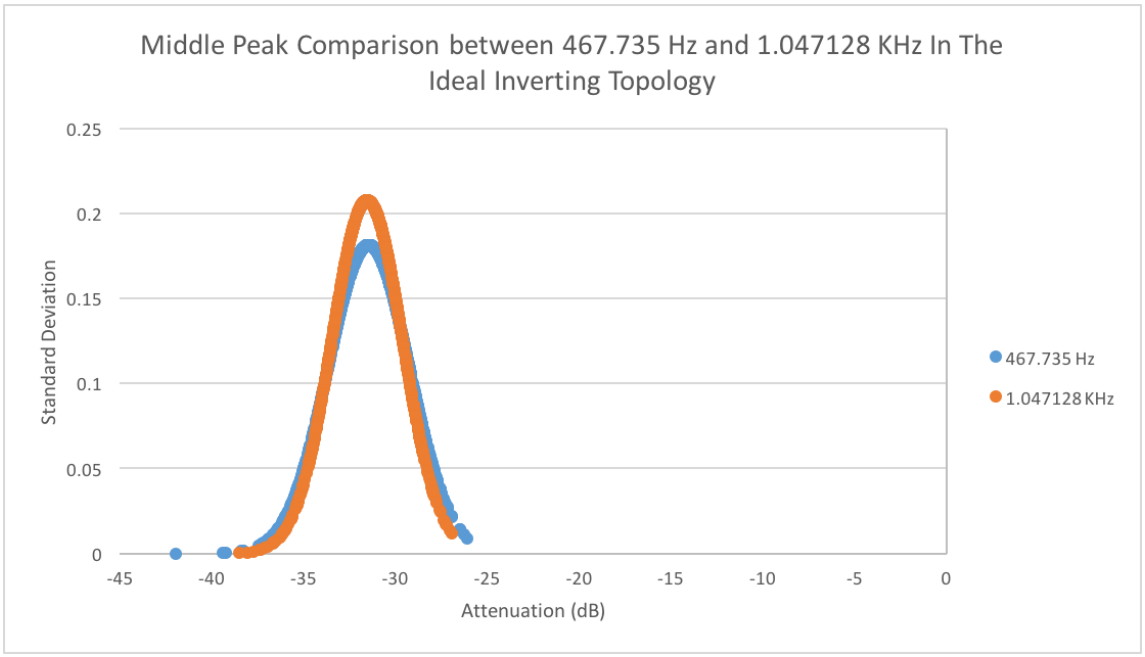

Figure 44. Comparison of middle peaks in a 5-stage filter implemented using Figure 40

Table 11. Comparison of attenuation and standard deviation of peak frequencies in the inverting topology

Peak	Average Attenuation (dB)	Standard Deviation (dB)
Edge Peak 1(213.796 Hz)	28.441	1.765
Edge Peak 2(2.344 KHz)	28.325	1.021
Middle Peak 1(467.735Hz)	31.463	2.198
Middle Peak 2(1.047 KHz)	31.544	1.920

Figure 43 and Figure 44 demonstrates how the five-stage filter that uses the "Inverting" topology compare to each other. At 213.796 Hz, the system has an average attenuation of 28.441 dB and a standard deviation of 1.765 dB. The other edge frequency, 2.344 KHz, has an average attenuation of 28.325 dB and a standard deviation 1.021. This shows that the lower edge lobe has a wider distribution that the higher frequency edge. The first middle peak has an attenuation of 31.463 dB and a standard deviation of 2.198 dB. At 1.047 KHz the system has an average attenuation of 31.544 dB and a standard deviation of 1.920 dB. At the higher middle lobe frequency, the standard deviation reduces. These two peaks are well matched.

From the results shown in the figure above, the inverting topology exhibits less sensitivity to component variation. The "Non-Inverting" topology lobes have much larger standard deviations than the inverting topology.

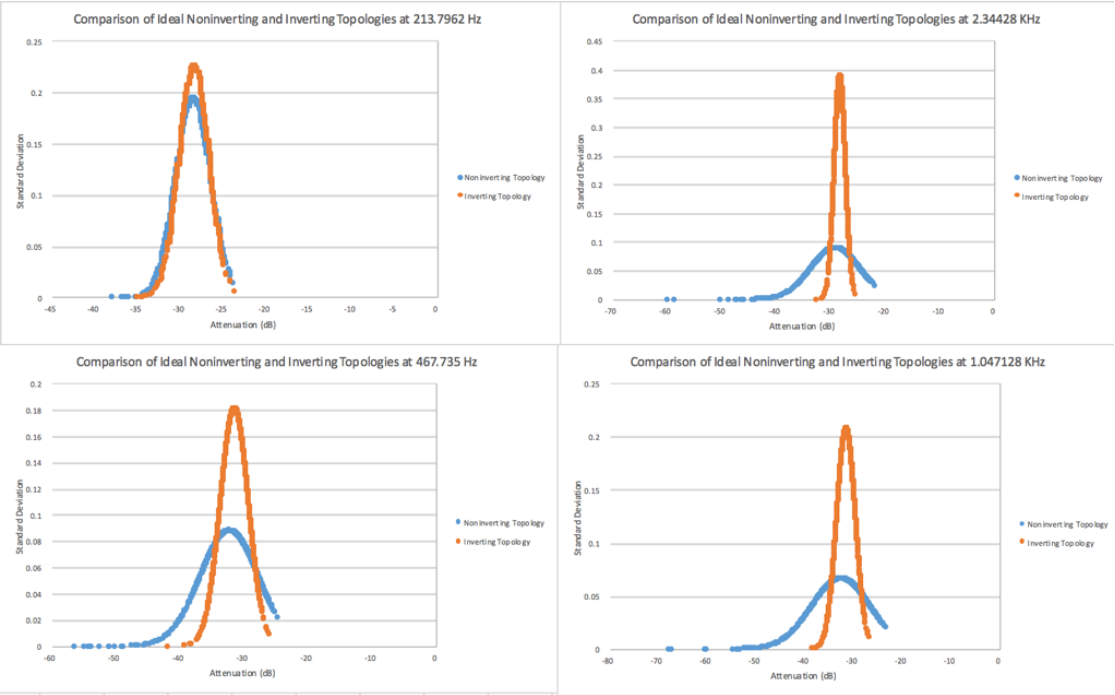

Figure 45. Comparison of peak frequencies between the ideal "Non-Inverting" (blue) and inverting (orange) topologies

Figure 45 demonstrates the effect component variation has on the two topologies at the frequencies of interest (lobe frequencies). The five stage filter that uses the "Non-Inverting" topology and the five stage filter that uses the "Inverting" topology have similar performance at 213.769 Hz, but at the higher frequency lobes, one can see the inverting topology has much less variation than the "Non-Inverting" topology.

5.2. Filter Stage Ordering

In an active cascade topology, the overall system transfer function corresponds to the product of the individual (stage) transfer functions. The overall system transfer function remains unchanged irrespective of stage ordering. This section explores if system robustness depends on stage order.

Previous research has shown that implementing a cascaded filter where each stage has a higher characteristic frequency than the previous stage does not always yield the best performance. In 5.1, the filter stages connect such that each stage has a higher characteristic frequency than the last. [4] found a particular stage ordering that improves overall system robustness.

Stage orderings in this section are denoted as 1-2-3-4-5 where each number corresponds to a filter stage. The 1 stage corresponds to the lowest characteristic frequency of interest and the following stages have increasing characteristic frequency locations over the previous stages. To simplify discussion of stage ordering the stage number refers to the stage that has a particular characteristic frequency location based upon the initial configuration.

5.2.1. 3-Stage System

To test all possible arrangement of the filter, set filter order to 3. With higher order systems, the number of ordering possibilities becomes very large; (N!) where N corresponds to the number of stages. A three-stage system yields 6 combinations of stage arrangements for each topology. This analysis looks at the attenuation floor (detailed in 4.2) of each topology and compares the results.

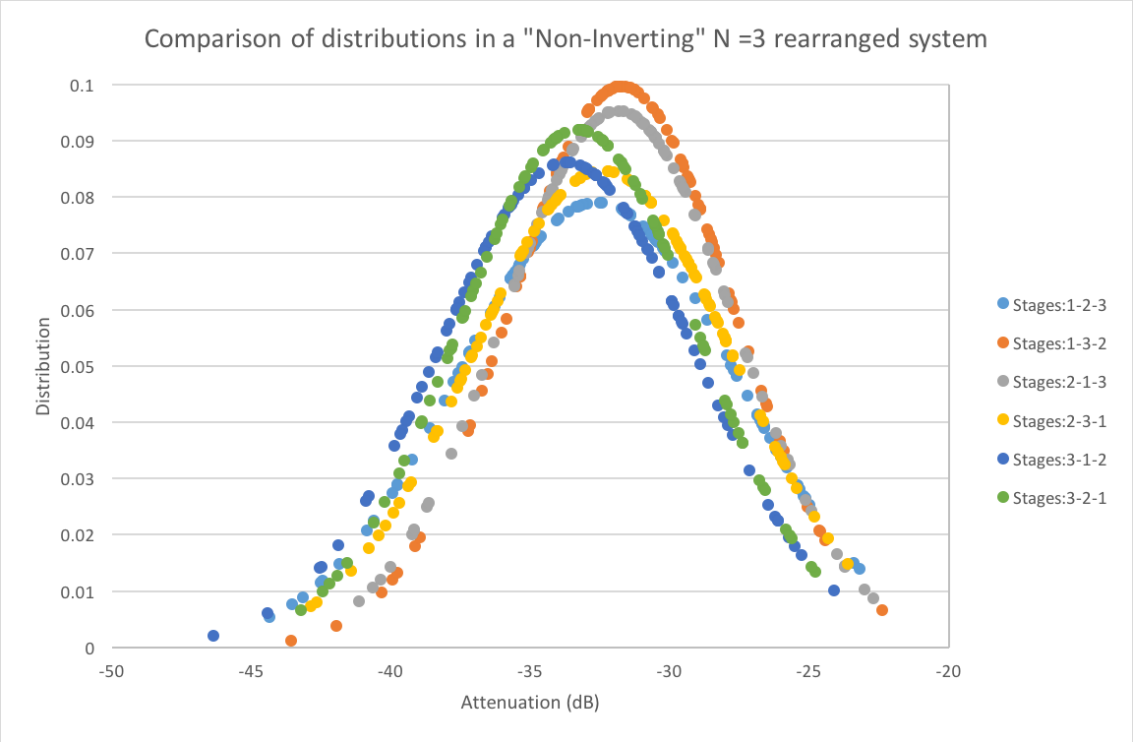

Figure 46. Comparison of distributions in a "Non-Inverting" N = 3 rearranged stage system, using ideal components

Figure 46 compares all six stage arrangement combinations of a "Non-Inverting" N = 3 cascaded system. This figure shows that the (1-2-3) and (1-3-2) stage configurations do not have the same performance as the other configuration arrangements. Arrangements (2-1-3), (2-3-1), (3-1-2), and (3-2-1) higher distribution of 0.25 dB centered around -24.5 dB. The (1-2-3) and (1-3-2) have a distributions of approximately 0.2 dB centered at -24 dB. The filter exhibits greater robustness when connected in the (2-1-3), (2-3-1), (3-1-2), and (3-2-1) orderings. The data presented in Figure 46 suggests that connecting the stages of the cascade in the descending characteristic frequency (3-2-1) configuration yields better robustness than connecting the filter in the ascending characteristic frequency (1-2-3) order.

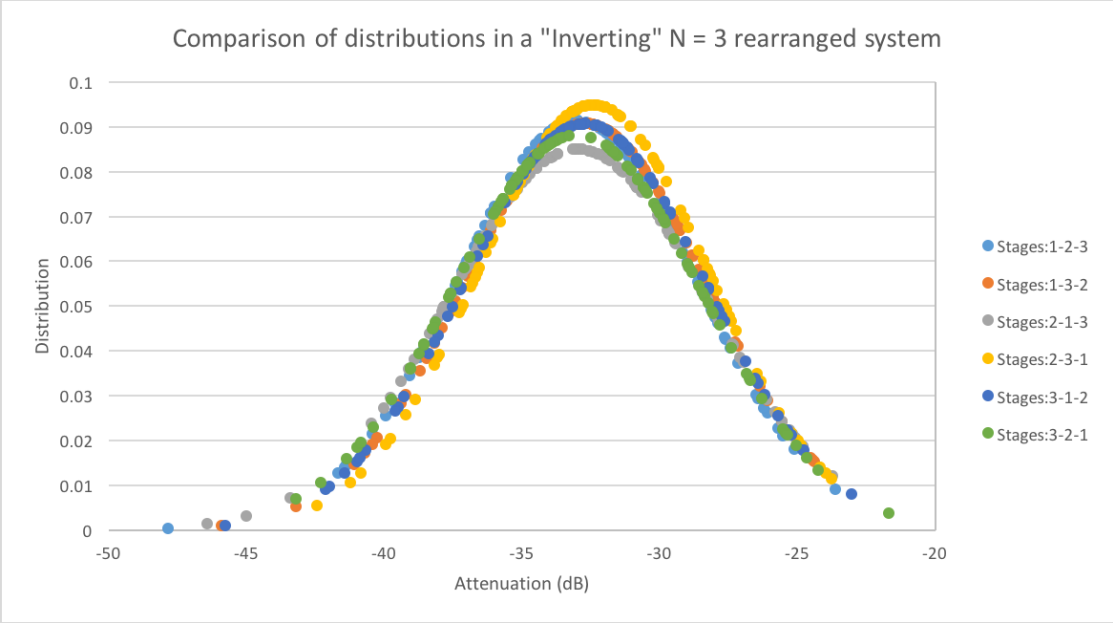

Figure 47. Comparison of distributions in an inverting N = 3 rearranged system, using ideal component values

Figure 47 shows a comparison of the normal distributions in an "Inverting" N = 3 cascade. The inverting cascade has a tighter spread than the normal distributions in Figure 46 for the "Non-Inverting" topology. The (1-2-3) and (2-3-1) have the highest distribution of approximately 0.25 dB centered around -24.5 dB. The responses from the (1-3-2) and (3-2-1) stage arrangements center around approximately -24.5 dB. The (3-2-1) and (2-1-3) arrangements have a distribution of 0.225 dB centered around -24 dB. From the data presented in Figure 47, connecting the stages of the cascade in the ascending characteristic frequency (1-2-3) configuration yields more robustness than connecting the filter in the descending characteristic frequency (3-2-1) order.

To accurately measure the performance of the reduced-op-amp topology, it becomes necessary to relate it to the buffered version of the Gingell RC-CR topology. This provides a "standard" comparison for the transfer characteristics and the robustness of the new topology. Figure 48 depicts the LTSpice schematic of the buffered Gingell RC-CR topology.

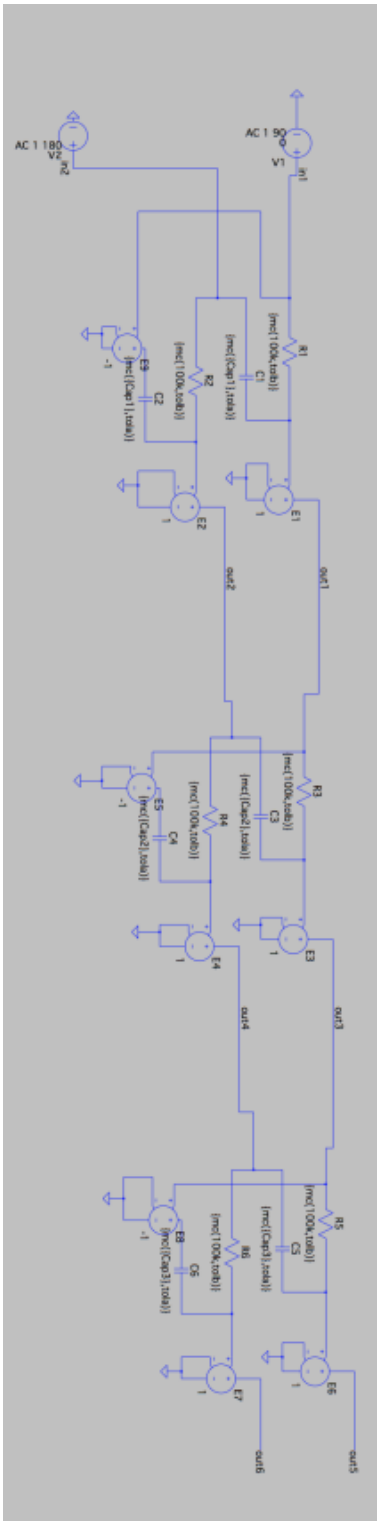

Figure 48. LTSpice schematic of buffered and cascaded Gingell's RC-CR topology

Resistor and capacitor values parameterize based on the notch frequency spacing value, k. The k value remains the same as the Gingell as the derived three stage "Non-inverting" topology; k = 1.38.

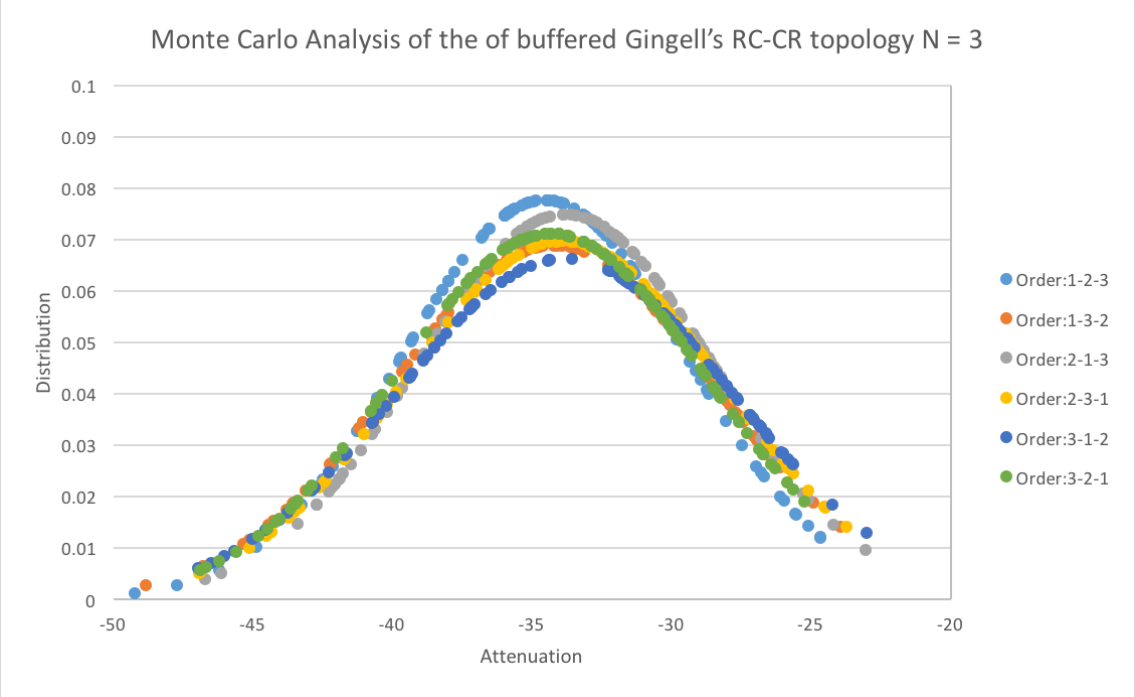

Figure 49. Comparison of distributions in a buffered Gingell RC-CR N = 3 rearranged system; k = 1.38

Figure 49 compares the different stage arrangements of a 3 stage buffered Gingell topology. The distribution has approximately 35 dB of attenuation and distribution peak of 0.08. The (1-2-3) arrangement exhibits the best performance. The (3-1-2) arrangement has the worst performance.

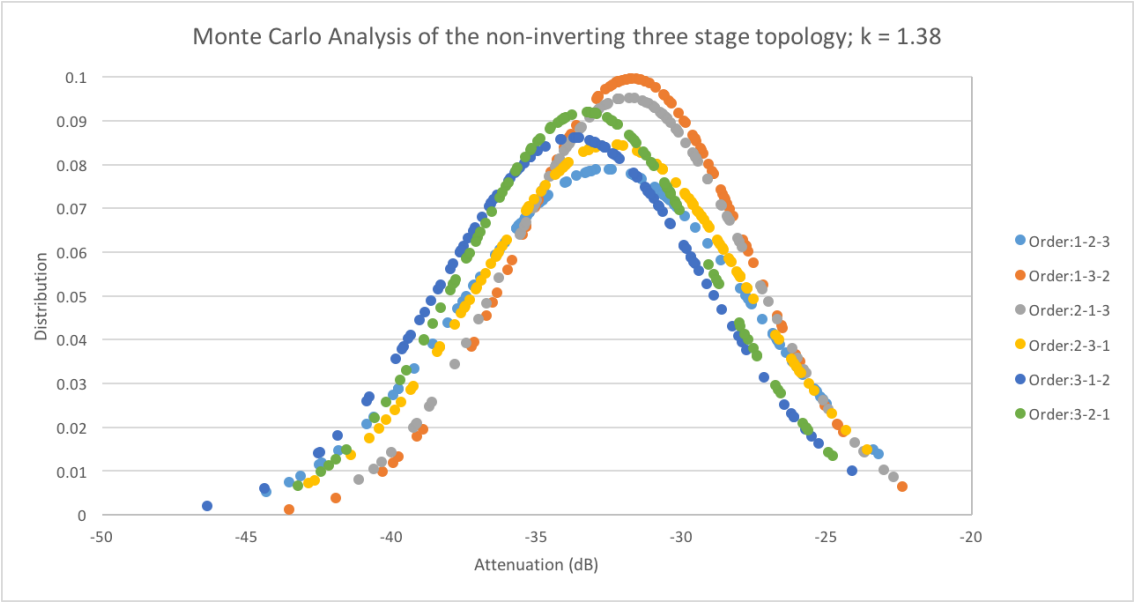

Figure 50. Monte Carlo Analysis of the "Non-Inverting" three stage topology; k = 1.38

Figure 50 shows the normal distributions of the arrangement of stages of an N = 3 "Non-Inverting" topology where k = 1.38. The distribution of this topology has more variation between arrangements than the active Gingell topology seen in Figure 49 and is centered on a lower attenuation, but has higher distribution peaks than the active Gingell topology.

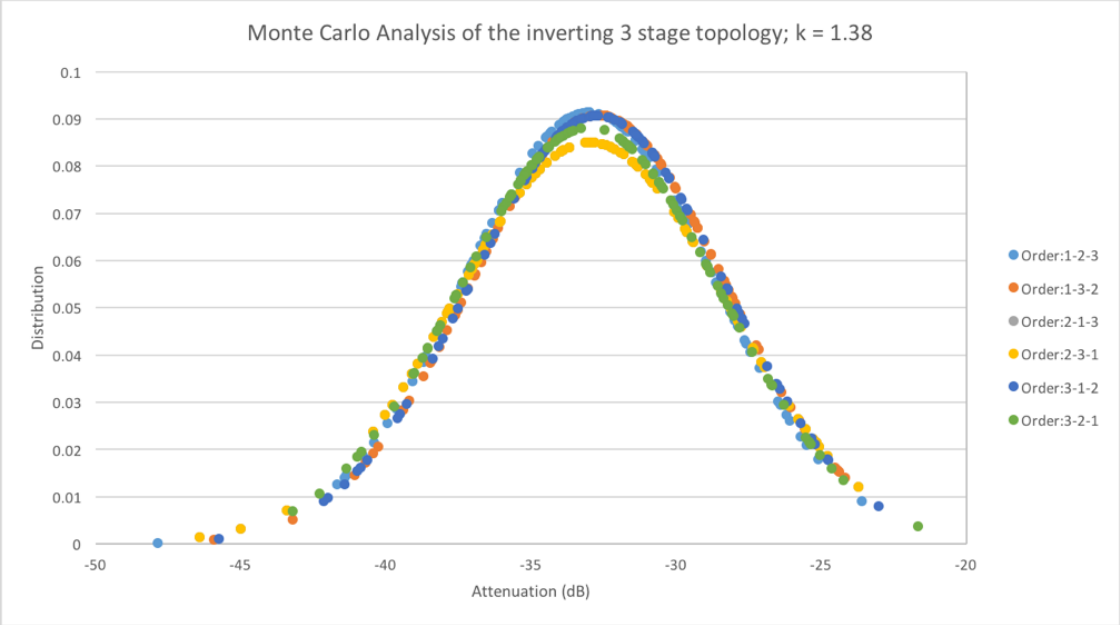

Figure 51. Monte Carlo Analysis of the "Inverting" three stage topology; k = 1.38

Figure 51 shows the distributions of the arrangement of stages of an N = 3 "Inverting" topology where k = 1.38. This topology has less overall variation when compared to the "Non-Inverting" topology, but is centered on a lower attenuation than the active Gingell topology. The "Inverting" topology has a distribution peak of 0.09 dB.

The results of this analysis shows that the distributions of the active Gingell topology performs comparably to the normal distributions of the "Non-Inverting" and "Inverting" topologies. Figure 50 and Figure 51 show that both topologies compare with the active Gingell topology.

5.2.2. 4-Stage System

The investigation of a N= 4 "Non-Inverting" topology determines if stage order impacts robustness. Because a 4-stage cascade has 24 different stage arrangements (based upon the N! relationship), the analysis uses only nine different cascade configurations. Using the results found in Chapter 5.2.1, the key configurations are the (1-2-3-4) and (4-3-2-1) arrangements.

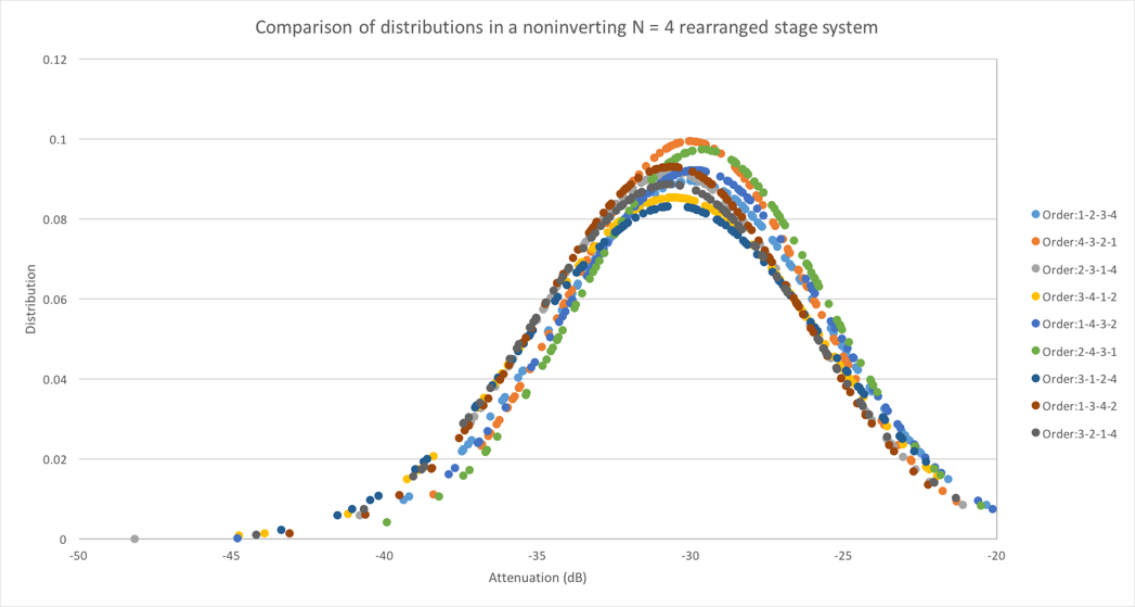

Figure 52. Comparison of distributions in a "Non-Inverting" N = 4 rearranged stage system, using ideal component values

Figure 52 compares the distribution of several arrangements of a "Non-Inverting" N = 4 stage filter. Increasing the order of the filter increases the attenuation (distribution center). In the 4 stage cascade, all distributions center around approximately -30dB. The arrangements that have the highest normal distributions are (2-4-3-1) and (4-3-2-1) and have a distribution peak of 0.1 dB. This shows that the data found in Chapter 5.2.1

applies to higher order filters as well. The “Non-Inverting” topology performs best when connected in a reverse order cascade.

5.2.3. 5-Stage System

The Monte Carlo analysis performed in 5.2.1 indicates that a “Non-Inverting” cascade exhibits the best performance when connected in a descending frequency order and the “Inverting” topology exhibits the best performance when connected in the standard ascending frequency arrangement. Chapter 5.2.2 shows that when filter order increases, the results found in 5.2.1 still apply. This section performs Monte Carlo on the five-stage cascade designed in Chapter 3.1 and the “Inverting” topology designed in Hay [19]. This investigation looks at each peak lobe in the stop-band response instead of looking at the overall highest attenuation point to better compare the performance of the filter cascades over the entire stopband.

This section explores the impact of cascading the “Non-Inverting” and “Inverting” topologies in reverse order; arranging characteristic frequencies from highest frequency to lowest frequency. In these configurations the peak frequencies shift slightly from the original configurations. The frequency peaks occur at 206.538 Hz, 469.894 Hz, 1.051 KHz, and 2.388 KHz.

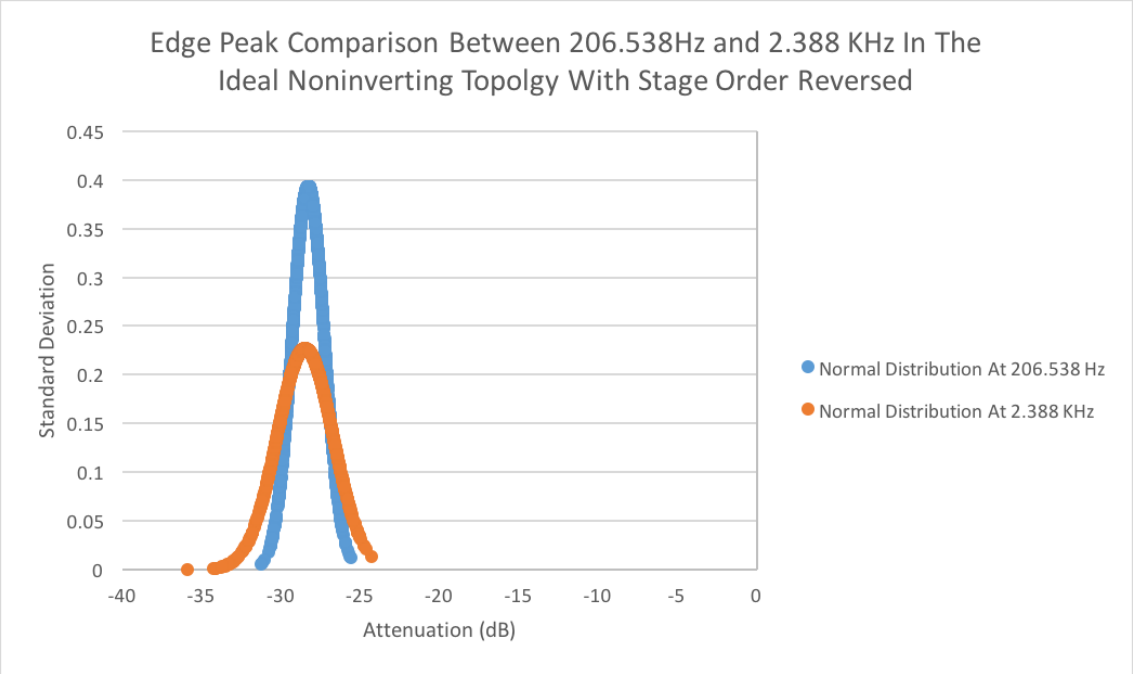

Figure 53. Comparison of edge peaks in a 5-stage filter implemented using reverse order of Figure 33, using ideal component values

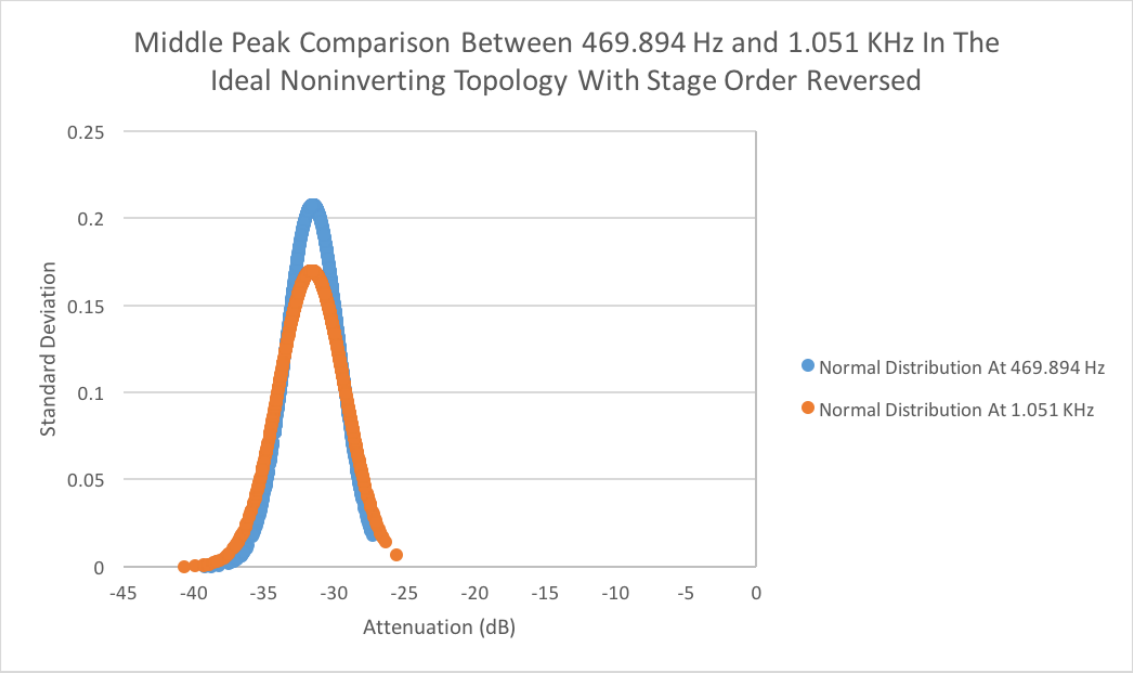

Figure 54. Comparison of middle peaks in a 5-stage filter implemented using a reverse order of Figure 33, using ideal component values

Table 12. Comparison of attenuation and standard deviation of peak frequencies in the "Non-Inverting" topology with stage order reversed

Peak	Average Attenuation (dB)	Standard Deviation (dB)
Edge Peak 1(206.528 Hz)	28.284	1.014
Edge Peak 2(2.388 KHz)	28.482	1.760
Middle Peak 1(469.894Hz)	31.545	1.922
Middle Peak 2(1.051 KHz)	31.622	2.350

Figure 53 compares the edge peaks and the middle peaks in the ideal "Non-Inverting" topology with the stage order reversed. This configuration exhibits much less variation than the standard "Non-Inverting" topology. In both configurations, the worst-case standard deviations occur at the second middle peak. In the standard configuration, the standard deviation is 5.982 dB. With the stage order reversed, the standard deviation is 2.350 dB.

The sensitivity of the "Non-Inverting" topology reduces dramatically by connecting the stages in reverse order. The system achieves performance similar to the standard inverting topology shown in Fig. 45.

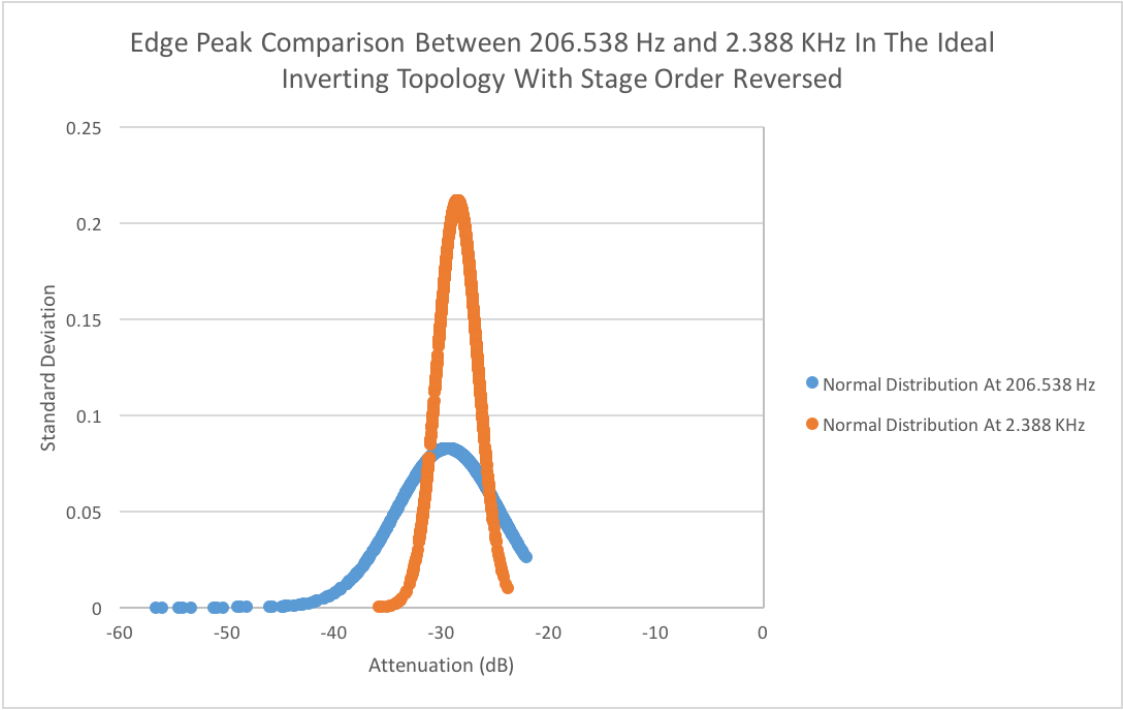

Figure 55. Comparison of edge peaks in a 5-stage filter implemented using a reverse order of Figure 40, using ideal component values

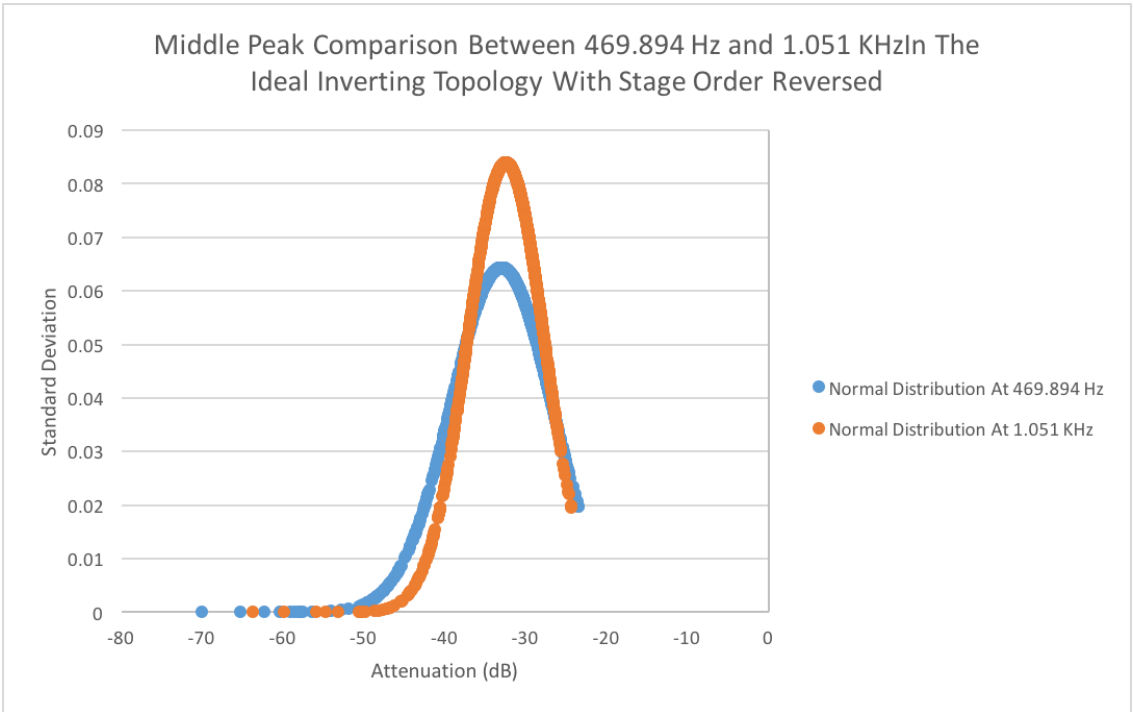

Figure 56. Comparison of middle peaks in a 5-stage filter implemented using a reverse order of Figure 40, using ideal component values

Table 13. Comparison of attenuation and standard deviation of peak frequencies in the inverting topology with stage order reversed

Peak	Average Attenuation (dB)	Standard Deviation (dB)
Edge Peak 1(206.538 Hz)	29.441	4.819
Edge Peak 2(2.388 KHz)	28.525	1.833
Middle Peak 1(469.894Hz)	33.032	6.200
Middle Peak 2(1.051 KHz)	32.488	4.753

Table 13 shows that for both edge and middle peaks, the higher frequency peaks exhibit less variation due to component tolerances. This matches the behavior seen in the standard "Inverting" topology. Connecting the "Inverting" topology in a reverse order the system yields more sensitivity to component variation than the standard cascade. The worst-case standard deviation occurs at the first middle peak in both configurations. In the standard configuration, the standard deviation is 2.198 dB. In the reverse order configuration, the standard deviation is 6.200 dB.

The results of this analysis show that by connecting the stages in a descending frequency order, the "Non-Inverting" topology exhibits less sensitivity to component variation and yields performance similar to the ideal inverting topology. If one wishes to use a "Non-Inverting" topology, they simply need to connect it in descending frequency order to improve the systems robustness to component variation.

In the case of the inverting topology with stage order reversed, sensitivity to component variation increases.

5.3. Component Matching

This section aims to illustrate the effect of component tolerances on the amount of attenuation produced by the cascaded system. This simulation utilizes a "Non-Inverting" N = 3 cascade in a (3-2-1) order to perform Mote Carlo analysis with different component tolerances – 1%, 3%, and 5%.

The initial study utilizes identical component tolerances; 1%, 3%, or 5%. Next, Monte Carlo analysis determines if using higher tolerance components in the first two stages and using 1% components in the third stage improves the distribution of the response when compared with the all higher tolerance configurations. Figure 57 shows simulation results.

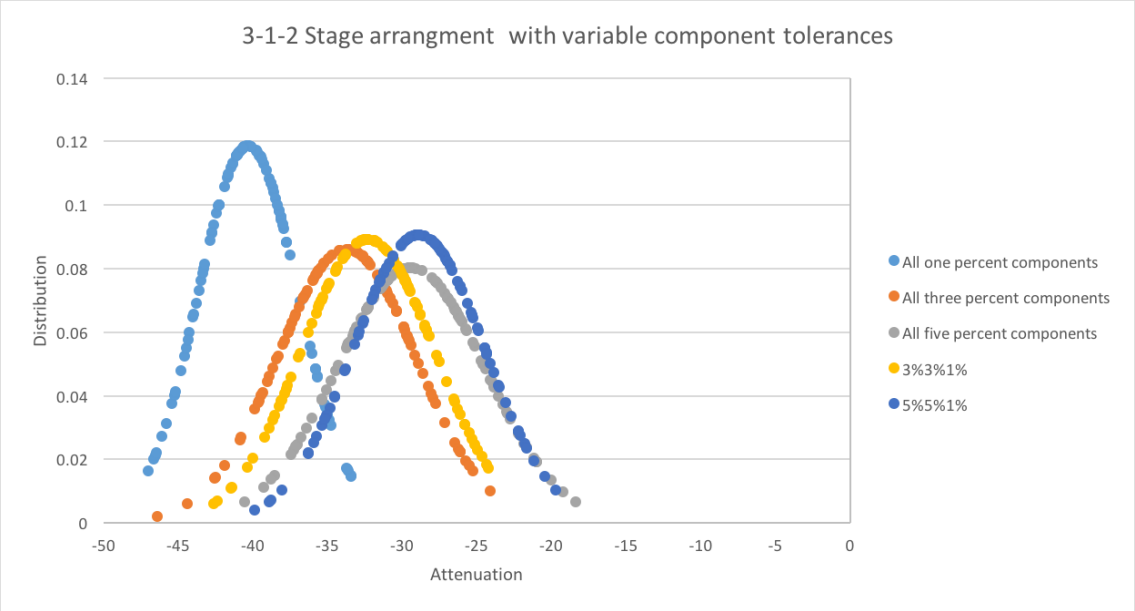

Figure 57. Non-inverting three stage topology with variable component tolerances

Using 1% components yields the best distribution response. The distribution centers around -42 dB and has a peak of 0.12. When tolerance values increases to 3%, the attenuation floor shifts to -34.8 dB and has a distribution of 0.085 dB. Increasing the tolerances to 5% further decreases the amount of expected attenuation to -27 dB with a distribution of 0.08 dB. This analysis shows a clear improvement using tighter tolerance components.

This research leads to the following observation. The amount of attenuation seen in a cascade depends upon component tolerance values.

$$Expected\ Attenuation \sim 20 * \log_{10}(\%component) \tag{5.1}$$

For example, using 1% components yields,

$$20 * \log_{10}(0.01) \sim -40\ dB \tag{5.2}$$

The measured attenuation floor equals 42 dB. Equation 5.2 shows that the approximate attenuation floor equals 40 dB. This equation serves as a "quick" method for determining the expected amount of attenuation given a certain percentage tolerance of components. This method of quickly determines design practicality given component tolerance. For example if a designer uses Equation 4.12, and calculates an attenuation of 60 dB; Equation 5.1 determines physical feasibility of a design specification with a given component tolerance. Using the result of equation 5.2, one percent components do not realize this attenuation goal.

This investigation did not test < 1% component tolerances because the investigation focuses on easily available and inexpensive components.

Monte Carlo analysis investigates two arrangements where the first two stages use 3% and 5% component values and the last stage in both networks uses 1% component tolerances. This determines if using 1% components in the final stage mitigate the effects of using lower tolerance components in the first two stages. Figure 57 shows that these arrangements do not increase the amount of attenuation that the distribution is centered around but does increase the height of the distribution peak. This shows that while using one percent components in the final stage does not dramatically change the overall response, it improves the robustness of the network, somewhat.

5.4. Summary of Monte Carlo Results

Chapter 5 performs extensive Monte Carlo analysis to determine the robustness of the topologies introduced in this thesis and in Hay [19]. The first Monte Carlo analysis investigates if the "Non-Inverting" topology or the "Inverting" topology has dramatically better performance than the other. Analysis found the "Inverting" topology performs better than the "Non-Inverting" topology. The next investigation determines if the arrangement of the cascade could improve the performance of both topologies. The result of this investigation found arrangements yielding better performance than others. The distributions of both topologies compare well with the active Gingell topology.

The Monte Carlo analysis in this chapter found that stage ordering does matter. The "best" ordering depends on the topology. For the multistage "Non-inverting" topology, the most robustness arrangement occurs in a descending characteristic frequency ordering and the multistage "Inverting" topology has the most robust response when connected in an ascending characteristic frequency ordering.

The largest finding of Chapter 5 is approximating filter performance based on the component tolerances used in a design; shown in Equation 5.1.

6. APPLICATIONS

6.1. Operation as a Phase Splitting Network

Figure 58 captures the magnitude response of the circuit when operated as a phase-splitter. Phase splitting output occurs by grounding one input and applying a sinusoid to the other.

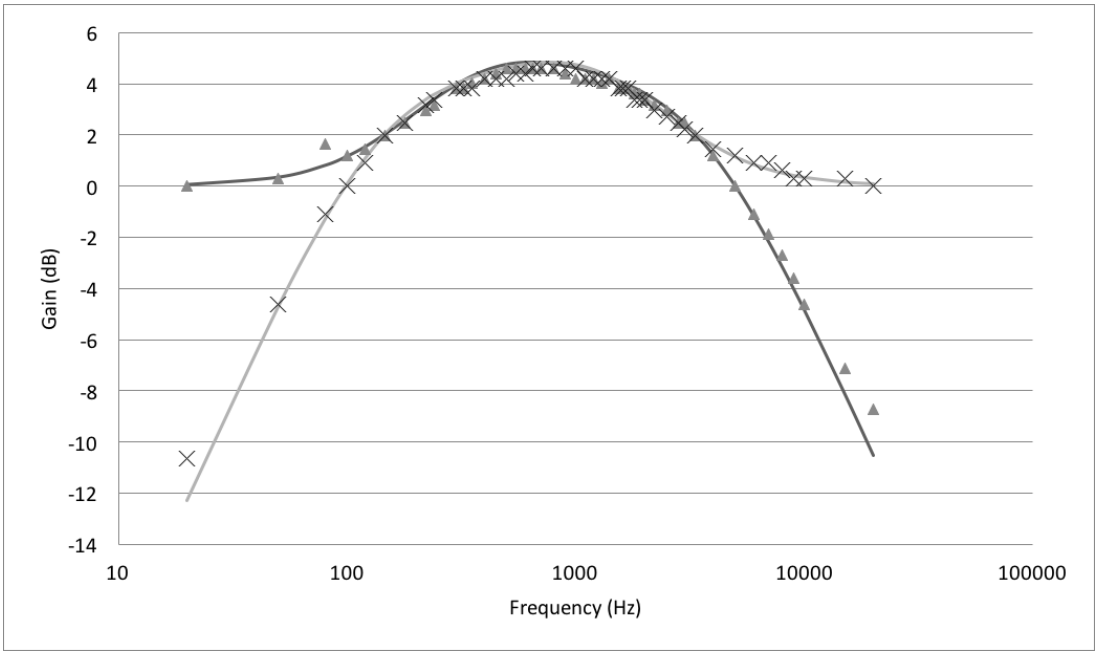

Figure 58. Filter magnitude response for phase-splitter operation

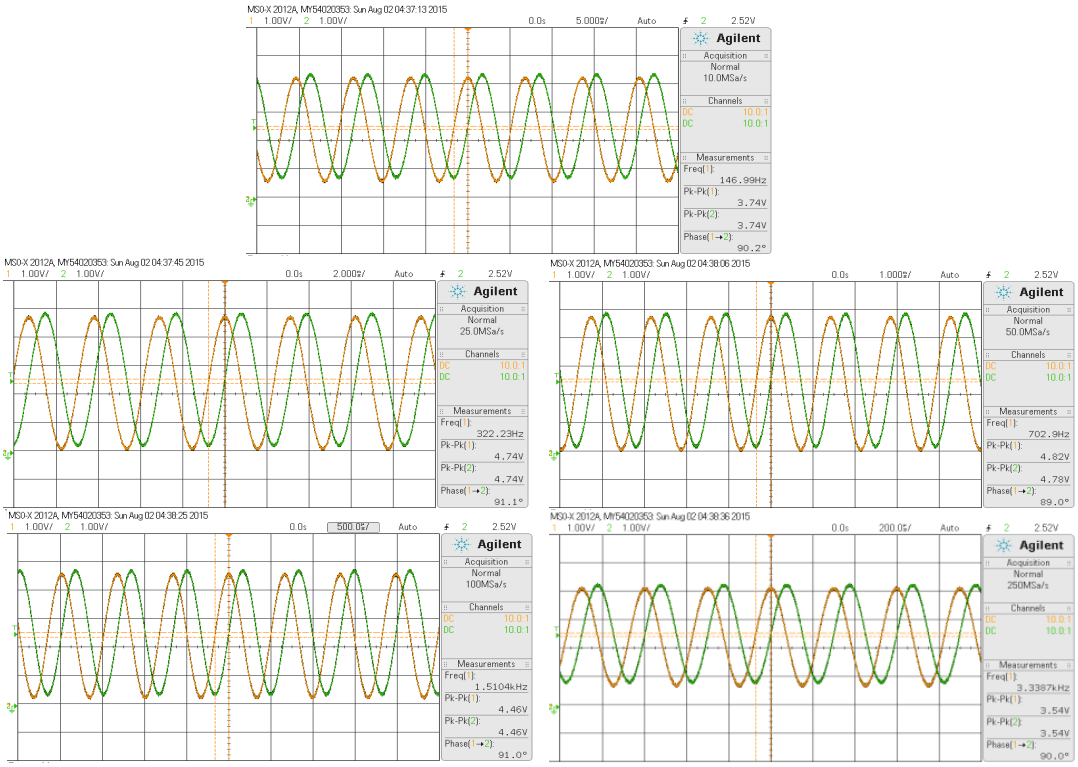

Figure 59. Non-inverting circuit outputs at calculated frequencies

Figure 59 shows the two outputs of the network in phase-splitter configuration. Each plot corresponds to the characteristic frequencies of each stage. These plots verify the phase splitting properties of the network over a large frequency range.

6.2. Alternative Waveform Visualization

The human brain is well suited for visual pattern recognition. Research has found that it takes the brain approximately 150 ms to process a complex image [20]. Due to the unique phase splitting characteristics of the topology developed in this thesis, an application of the network connects each output of the network to two inputs of an oscilloscope in XY mode. A sinusoidal input to the network creates two output sinusoids 90-degrees out of phase with other. Connecting an oscilloscope in XY mode to the two outputs displays a circle.

Figure 60 through Figure 77 present a number of time domain waveforms and their XY counterparts. The purpose of this section presents examples of visualizing traditional waveforms in an alternative fashion. These responses have applications in visual signal pattern recognition.

Input Sine 560Hz, 1Vpp, 2.5DC Offset

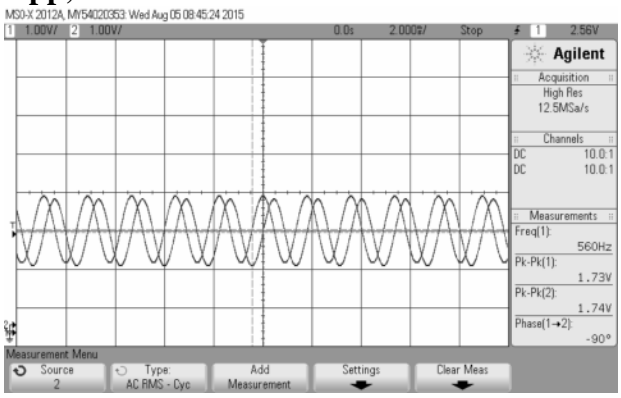

Figure 60. Hilbert pair of signals produced by Input: Sine 560Hz, 1Vpp, 2.5DC Offset - Time Domain

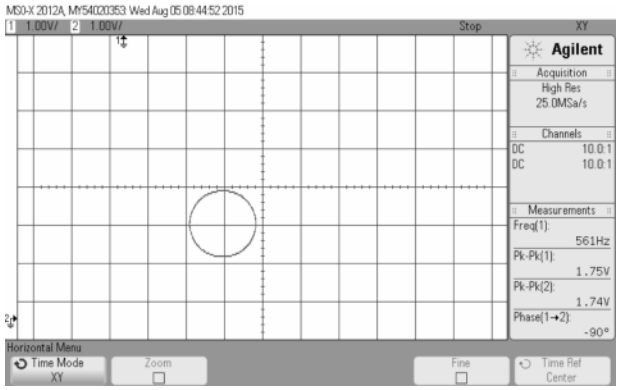

Figure 61. *Hilbert pair from Figure 60 displayed as parametric x-y plot*

Input Square 560Hz, 1Vpp, 2.5DC Offset, 50%Duty

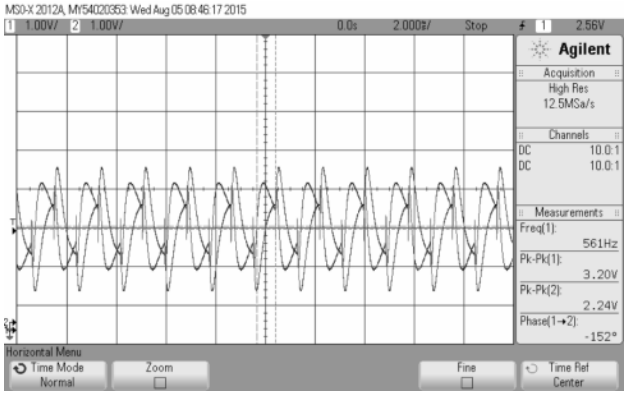

Figure 62. Hilbert pair of signals produced by Input: Square 560Hz, 1Vpp, 2.5DC Offset, 50% Duty Cycle -Time Domain

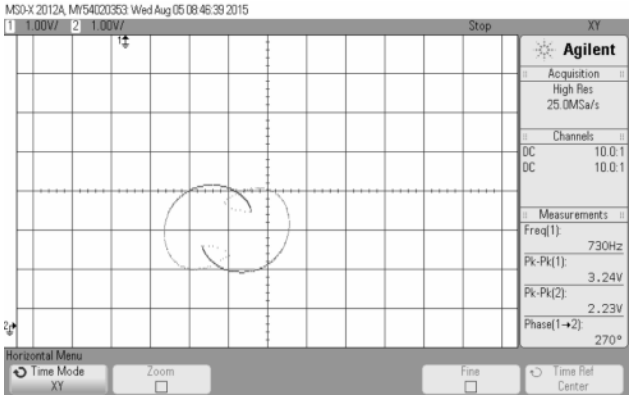

Figure 63. Hilbert pair from Figure 62 displayed as parametric x-y plot

Input Ramp 560Hz, 1Vpp, 2.5DC Offset, 100% Symmetry

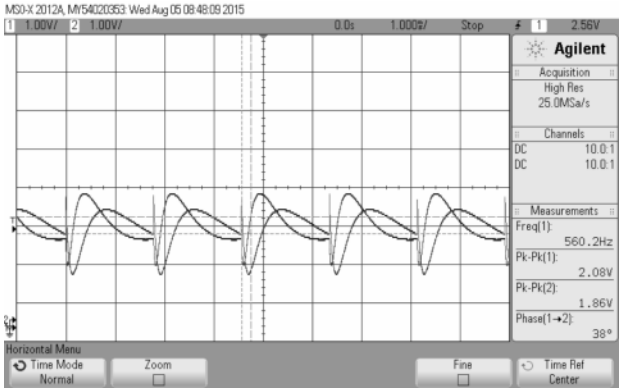

Figure 64. Hilbert pair of signals produced by Input: Ramp 560Hz, 1Vpp, 2.5DC Offset, 100% Symmetry - Time Domain

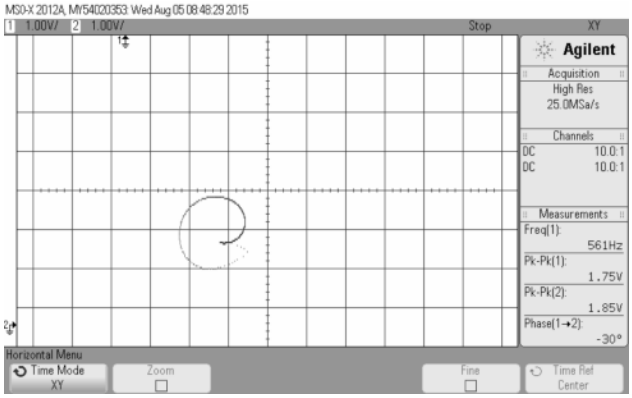

Figure 65. Hilbert pair from Figure 64 displayed as parametric x-y plot

Input Pulse 560Hz, 1Vpp, 2.5DC Offset, 50% Duty

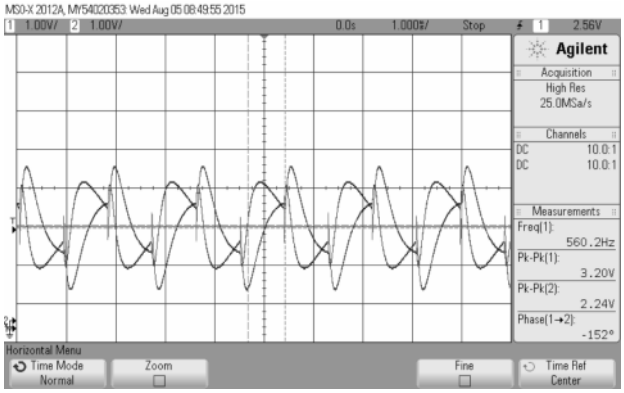

Figure 66. Hilbert pair of signals produced by Input: Pulse 560Hz, 1Vpp, 2.5DC Offset, 50% Duty Cycle - Time Domain

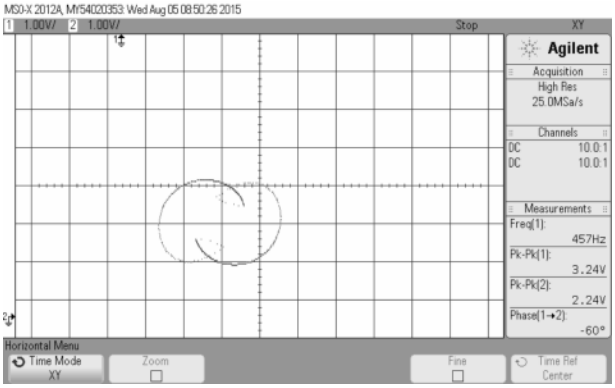

Figure 67. Hilbert pair from Figure 66 displayed as parametric x-y plot

Input Noise 4.8Vpp, 2.5VDC Offset

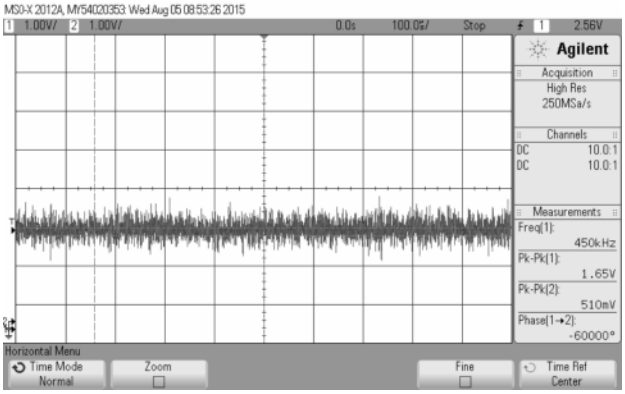

Figure 68. Hilbert pair of signals produced by Input: Noise 4.8Vpp, 2.5VDC Offset - Time Domain

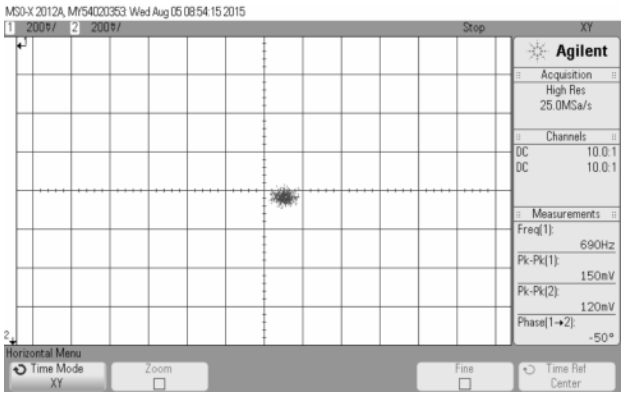

Figure 69. Hilbert pair from Figure 68 displayed as parametric x-y plot

Input Sinc 560Hz, 1Vpp, 2.5DC Offset

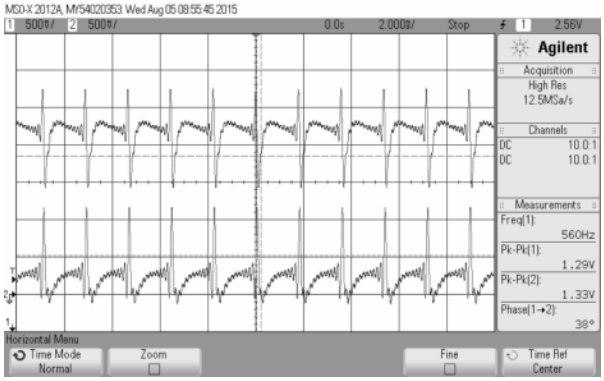

Figure 70. Hilbert pair of signals produced by Input: Sinc 560Hz, 1Vpp, 2.5DC Offset - Time Domain

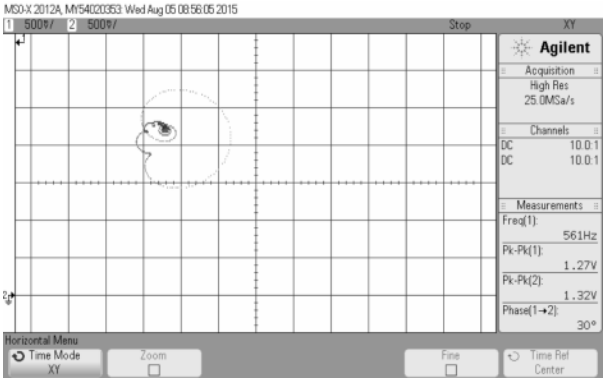

Figure 71. Hilbert pair from Figure 70 displayed as parametric x-y plot

Input Gaussian Pulse 560Hz, 1Vpp, 2.5DC Offset

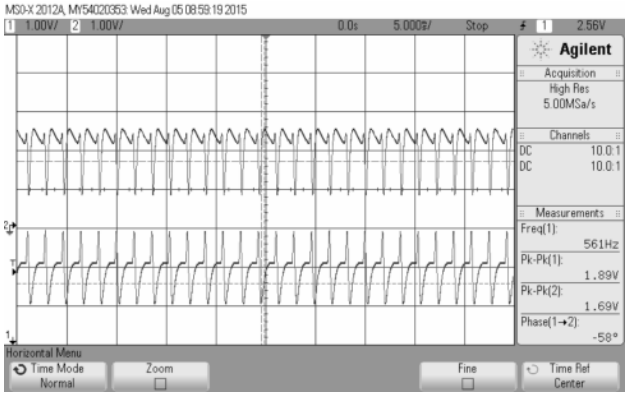

Figure 72. Hilbert pair of signals produced by Input: Gaussian Pulse 560Hz, 1Vpp, 2.5DC Offset - Time Domain

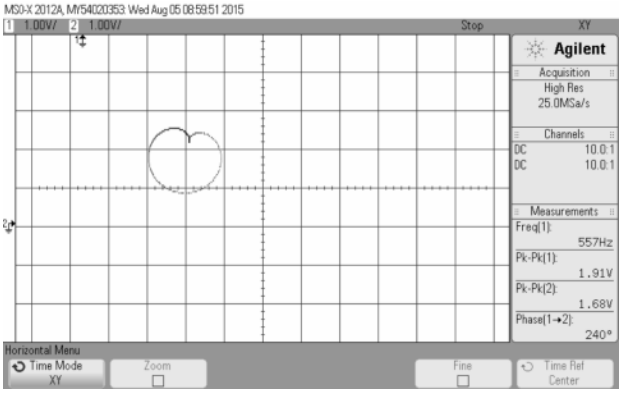

Figure 73. Hilbert pair from Figure 72 displayed as parametric x-y plot

Input Voice 560Hz, 1Vpp, 2.5DC Offset

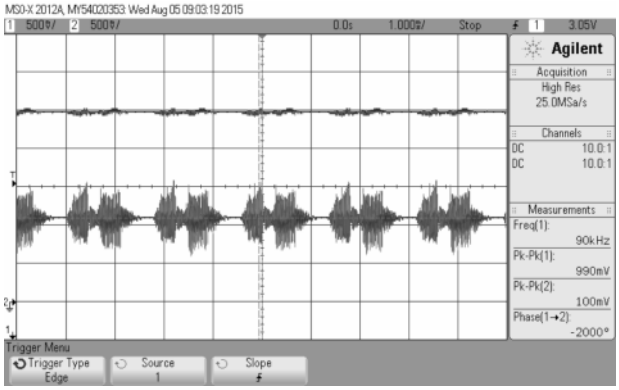

Figure 74. Hilbert pair of signals produced by Input: Voice 560Hz, 1Vpp, 2.5DC Offset - Time Domain

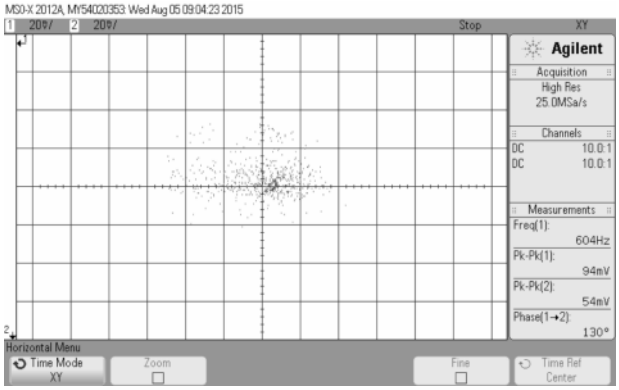

Figure 75. Hilbert pair from Figure 74 displayed as parametric x-y plot

Input Cardiac 560Hz, 1Vpp, 2.5DC Offset

Figure 76. Hilbert pair of signals produced by Input: Cardiac 560Hz, 1Vpp, 2.5DC Offset - Time Domain

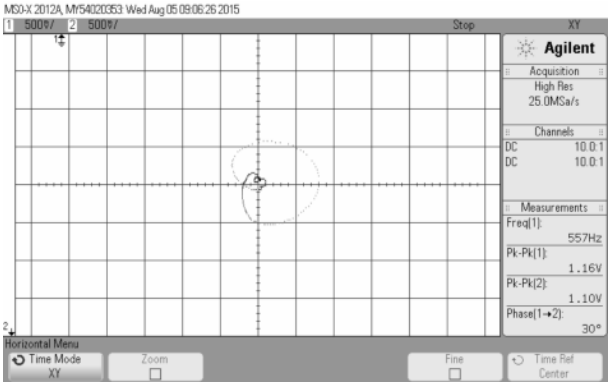

Figure 77. Hilbert pair from Figure 76 displayed as parametric x-y plot

7. CONCLUSION AND FUTURE WORK

This thesis creates an active Complex Filter that requires two op-amps. The Complex Filter exhibits a frequency asymmetric property that responds differently to input sequences that have either a positive 90-degree phase difference or a negative 90-degree phase difference. When the input sequence has a positive 90-degree phase difference, the filter has a band-pass response and when the input sequence has a negative 90-degree phase difference, the system has a band-stop response. This discussion focuses heavily on the design of a Complex Filter from the band-stop perspective. In a cascade, each stage contributes a notch response that changes attenuation seen in the stopband. The spacing of the notch locations contributed by each stage leads to the derivation of equations that approximate stop-band attenuation.

The robustness of the topology developed in this thesis and the topology developed in Hay [19] is investigated using Monte Carlo Analysis. The analysis found the "Non-Inverting" topology becomes most robust when connected with decreasing characteristic frequencies. The most robust "Inverting" topology occurs when connected with increasing characteristic frequencies. Component tolerances determine approximate system attenuation.

Future work includes the application of the phase-splitting properties of the Complex Filter derived in this thesis. The analysis found in Chapter 6.2 presents a variety of time domain signals and their XY counterparts to highlight waveform visualization applications. The XY representation has the potential for applications in signal processing where patterns lost in the time domain representation become apparent.

BIBLIOGRAPHY

[1] M. GINGELL, "Single Sideband Modulation using Sequence Asymmetric Polyphase Networks," Standard Telecommunication Laboratories Limited, Harlow. England, 1973.

[2] R. Jaeger and T. Blalock, "Microelectronic Circuit Design," NEw York, McGraw Hill, 2011, pp. 650-653.

[3] K. Martin, "Complex Signal Processing is Not Complex," *IEEE TRANSACTIONS ON CIRCUITS AND SYSTEMS,* vol. 51, no. 9, pp. 1823-1836, 2004.

[4] P. Kiss, V. Prodanov and J. Glas, "COMPLEX LOW-PASS FILTERS," *IEEE,* vol. 7803, no. 7448, pp. 525-528, 2002.

[5] L. Z. W. R. a. O. F. Fayrouz Haddad, Mobile and Wireless Communications Network Layer and Circuit Level Design, Rijeka: INTECH, 2010.

[6] S. Darlington, "Realization of a Constant Phase Difference," *Bell System Technical Journal* , 17 4 1950.

[7] W. Saraga, "The Design of Wide-Band Phase Splitting Networks," *PROCEEDINGS OF THE I.R.E.,* pp. 754-770, July 1950.

[8] H. Howard and A. Faries, "A CONSTANT PHASE-DIFFERENCE NETWORK AND ITS APPLICATIONS TO A FILTER FOR AMATEUR-TYPE TRANSMITTER," LELAND STANFORD JUNIOR UNIVERSITY, STANFORD, 1955.

[9] S. BEDROSIAN, "NORMALIZED DESIGN OF 90-DEGREE PHASE-DIFFERENCE NETWORKS," *IRE TRANSACTIONS ON CIRCUIT THEORY,* pp. 128-136, JUNE.

[10] D. Sinisa, "An AF All pass Quadrature Networks Practical Approach old Technique Revised," Belgrade, 2006.

[11] B. Hutchins, "THE DESIGN OF WIDEBAND ANALOG 90-DEGREE PHASE DIFFERENCING NETWORKS WITHOUT A LARGE SPREAD OF CAPACITOR VALUES".

[12] E. Stikvoort, "Polyphase Filter Section With OPAMPs," *IEEE TRANSACTIONS ON CIRCUITS AND SYSTEMS—II: ANALOG AND DIGITAL SIGNAL PROCESSING,* vol. 50, no. 6, pp. 376-378, 2003.

[13] W. Wiebach, "DESIGN AND ANALYSIS OF 90-DEGREE PHASE DIFFERENCE NETWORKS," National Technical Information Service, Springfield Va..

[14] M. Feldman, "Hilbert transform in vibration analysis," *Mechanical Systems and Signal Processing,* vol. 25, pp. 735-802, 2010.

[15] Y.-W. Liu, "Hilbert Transform and Applications," 2012. [Online]. Available: www.intechopen.com. [Accessed 01 05 2016].

[16] W. Freeman, "Hilbert transform for brain waves," 21 7 2013. [Online]. Available: www.scholarpedia.org/article/Hilbert_transform_for_brain_waves. [Accessed 20 6 2015].

[17] M. Johansson, "The Hilbert transform," VaÄxjÄo University, N/A.

[18] A. S. House, "Formant band widths and vowel preference," *Journal of Speech and Hearing Reseach ,* vol. 3, no. 1, 1960.

[19] N. M. Hay, "Complex Filters as cascade of Buffered Gingell structures: Design from Band-Pass Constraints," San Luis Obispo, 2016.

[20] S. Thorpe, D. Fize and C. Marlot, "Speed of processing in the human visual system," *LETTERS TO NATURE,* vol. 381, no. 6, pp. 520-522, 1996.

[21] V. LARROWE, "BAND-PASS QUADRATURE FILTERS," *IEEE TRANSACTIONS ON ELECTRONIC COMPUTERS,* Vols. EC-15, no. 6, pp. 726-731, 1966.

[22] W. Hartman, "Some psychoacoustical experiments with all-pass networks," Physics Department Michigan State University, East Lansing, Michigan, 1978.

[23] A. AMBARDAR, ANALOG AND DIGITAL SIGNAL PROCESSING, Pacific Grove, CA: Brooks/Cole Publishing Company, 1999.

APPENDICES

A. Complex Sequence

Complex number notation, x+jy, describes a rotating vector. This notation has a complex exponential representation. A counter-clock-wise rotating vector (Figure 78,a) with a fixed magnitude and angular rate of change expressed in complex notation corresponds to:

$$\frac{A}{\sqrt{2}} * \cos(\omega * t) + j * \frac{A}{\sqrt{2}} * \sin(\omega * t) = A * e^{j\omega t} \quad \text{(A.1)}$$

Similarly, a clock-wise rotating vector in complex number notation correspond to:

$$\frac{A}{\sqrt{2}} * \cos(\omega * t) - j * \frac{A}{\sqrt{2}} * \sin(\omega * t) = A * e^{-j\omega t} \quad \text{(A.2)}$$

Extending the same notation to real-valued functions, for a cosine results in the following equation:

$$A * \cos(\omega * t) + j * 0 = \frac{A}{2} * e^{j\omega t} + \frac{A}{2} * e^{-j\omega t} \quad \text{(A.3)}$$

Euler's equation describes equation A.3 [21,16].

To examine a clock-wise case, exchange the x and the y components, represented in Figure 78, b.

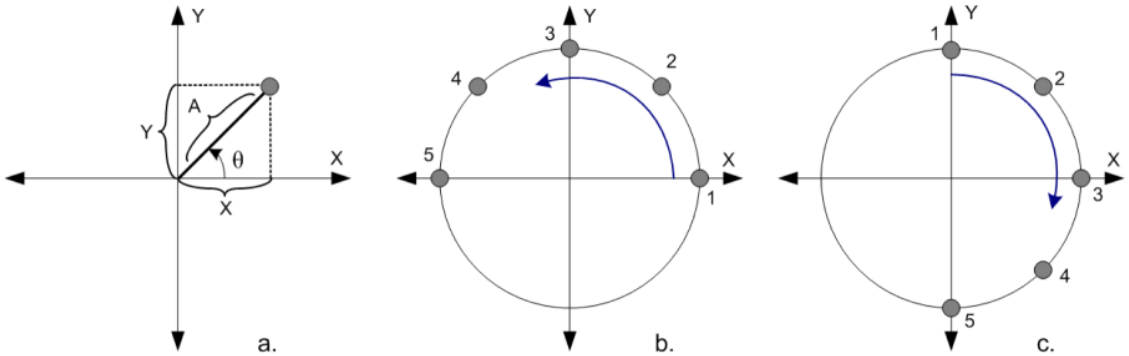

Figure 78. Component definition and rotation direction definition in the S-plane, a. X and Y components of a rotating vector, b. Clock-wise (positive) rotation, c. Counter clock-wise (negative) rotation

Table 14 and Table 15 illustrate the resulting vector angle from X and Y components given a particular component angle. This proves that interchanging the X component and Y component (counter-clock-wise case) results a change in the direction of the vector's rotation, which corresponds to change in the sign of the angular frequency.

Table 14. X = cos θ, Y = sin θ, X + jY = e^ϕ

Position (Fig. 1, b)	**θ(˚)**	**ϕ(˚)**
1	0	0
2	45	45
3	90	90
4	135	135
5	180	180

Table 15. X = sin θ, Y = cos θ, X + jY = e^ϕ

Position (Fig. 1, c)	**θ (˚)**	**ϕ(˚)**
1	0	90
2	45	45
3	90	0
4	135	-45
5	180	-90

B. Positive and Negative Frequencies

Frequency describes periodic behavior. The concept of positive and negative frequencies requires more explanation.

To better understand “Negative frequency”, consider how the concept of frequency relates to a rotating vector. Angular frequency, magnitude, and direction describe any rotating vector. Angular frequency is measured in radians-per-second and describes how fast the vector rotates. “Positive” and “negative” describe the direction of rotation. A vector rotating in the counter-clockwise direction, Figure 78 b, corresponds to a positive frequency. A clockwise rotating Figure 78 c, would have a negative frequency.

Figure 78, shows the end point of a rotating vector. This point traces a circle. Using Cartesian coordinates as a pair of sinusoids. A vector rotating in the counter-clockwise direction with an angular frequency of ω has the parametric description described below.

$$x(t) = \frac{A}{\sqrt{2}} * \cos(\omega * t) \tag{B.1}$$

$$y(t) = \frac{A}{\sqrt{2}} * \sin(\omega * t) \tag{B.2}$$

A clockwise rotating vector has the following parametric description.

$$x(t) = \frac{A}{\sqrt{2}} * \cos(\omega * t) \tag{B.3}$$

$$y(t) = -\frac{A}{\sqrt{2}} * \sin(\omega * t) \tag{B.4}$$

Rewrite the description as:

$$x(t) = \frac{A}{\sqrt{2}} * \cos(-\omega * t) \tag{B.5}$$

$$y(t) = \frac{A}{\sqrt{2}} * \sin(-\omega * t) \tag{B.6}$$

This shows that changing the direction of rotation changes the sign of the frequency.

Any sinusoidal pair corresponds to a sum of positive and negative frequency sequences.

For example:

$$V_{in1}(t) = \cos(\omega * t) \tag{B.7}$$

$$V_{in2}(t) = 0 \tag{B.8}$$

Expressed as

$$V_{in1}(t) = \frac{1}{2}\cos(\omega * t) + \frac{1}{2}\cos(\omega * t) \tag{B.9}$$

$$V_{in2}(t) = \frac{1}{2}\sin(\omega * t) + (-\frac{1}{2}\sin(\omega * t)) \tag{B.10}$$

The positive sequence corresponds to $\frac{1}{2}\cos(\omega * t)$ and $\frac{1}{2}\sin(\omega * t)$ and the negative sequence corresponds to $\frac{1}{2}\cos(\omega * t)$ and $-\frac{1}{2}\sin(\omega * t)$.

C. Derivation of Complex Topology in Figure 11 by superposition

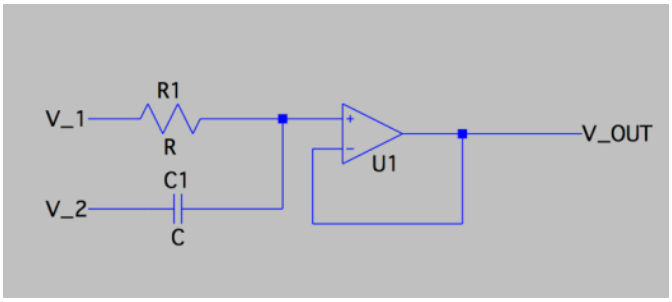

Figure 79. Active RC low pass filter

For V_2 grounded:

$$\frac{V_{OUT1} - V_1}{R} + \frac{V_{OUT1} - 0}{\frac{1}{s * c}} = 0$$

$$\frac{V_{OUT1} - V_1 + V_{OUT1} * s * C * R}{R} = 0$$

$$V_{OUT1}(1 + s * C * R) = V_1$$

$$H_1 = \frac{V_{OUT}}{V_1} = \frac{1}{1 + s * C * R}$$

For V_1 grounded:

$$\frac{V_{OUT2} - V_2}{\frac{1}{s * C}} + \frac{V_{OUT2} - 0}{R} = 0$$

$$\frac{(V_{OUT2} - V_2) * R + V_{OUT2} * \frac{1}{s * C}}{\frac{1}{s * C} * R} = 0$$

$$V_{OUT2} * R - V_2 * R + V_{OUT2} * s * C = 0$$

$$V_{OUT2}(R + \frac{1}{s * C} = V_2 * R$$

$$H_2 = \frac{V_{OUT2}}{V_2} = \frac{R}{R + \frac{1}{s * C}} = \frac{1}{\frac{R * s * C + 1}{s * C}} = \frac{R * s * C}{R * s * C + 1}$$

V_{OUT}:

$$V_{OUT} = H_1(s) * V_1 + H_2(s) * V_2 = \frac{1}{1 + s * C * R} * V_1(s) + \frac{s * C * R}{1 + s * C * R} * V_2(s)$$

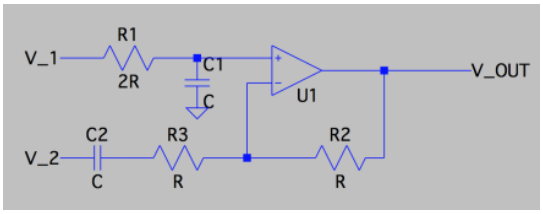

Figure 80. 2-input topology realizes LP TF with respect to v1 and inverting HP with respect to v2

For V_2 grounded:

$$\frac{V_+ - V_1}{2 * R} + \frac{V_+ - 0}{\frac{1}{s * C}} = 0$$

$$\frac{V_+ - V_1}{2 * R} + V_+ * s * C = 0$$

$$V_+ - V_1 + V_+ * s * C * 2R = 0$$

$$V_+(1 + s * C * 2R) = V_1$$

$$V_+ = \frac{V_1}{1 + s * C * 2R} = V_-$$

$$V_+ = V_-$$

$$\frac{V_- - V_{OUT1}}{R} + \frac{V_- - 0}{R + \frac{1}{s * C}} = 0$$

$$\frac{V_- - V_{OUT1}}{R} + \frac{V_-}{\frac{R * s * C + 1}{s * C}} = 0$$

$$\frac{V_- - V_{OUT1}}{R} + \frac{V_- * s * C}{R * s * C + 1} = 0$$

$$\frac{V_- - V_{OUT1}}{R} = -\frac{V_- * s * C}{R * s * C + 1}$$

$$V_-(s * C * R + 1) - V_{OUT1}(s * C * R + 1) = -V_-(s * C * R)$$

$$V_-(s * C * R + 1) + V_-(s * C * R) = V_{OUT1}(s * C * R + 1)$$

$$V_{OUT1} = \frac{V_-(s*C*R+1) + V_-(s*C*R)}{(s*C*R+1)}$$
$$= \frac{\frac{V_1}{1+s*C*2R}(s*C*R+1) + \frac{V_1}{1+s*C*2R}(s*C*R)}{(s*C*R+1)}$$

$$H_1 = \frac{V_{OUT1}}{V_1} = \frac{\frac{1+s*C*R}{1+s*C*2R} + \frac{s*C*R}{1+s*C*2R}}{1+s*C*R} = \frac{\frac{1+s*C*R+s*C*R}{1+s*C*2R}}{1+s*C*R}$$
$$= \frac{1}{1+s*C*R}$$

For V_1 grounded:

$$\frac{V_- - V_2}{\frac{R*s*C+1}{s*C}} + \frac{V_- - V_{OUT2}}{R} = 0$$

$$\frac{V_-*s*C - V_2*s*C}{R*s*C+1} + \frac{V_- - V_{OUT2}}{R} = 0$$

$$\frac{V_-*s*C - V_2*s*C}{R*s*C+1} = -\frac{V_- - V_{OUT2}}{R}$$

$$V_-*s*C*R - V_2*s*C*R = -V_-*(R*s*C+1) + V_{OUT2}(R*s*C+1)$$

$$V_- = 0$$

$$-V_2*s*C*R = V_{OUT2}*(1+s*C*R)$$

$$H_2 = \frac{V_{OUT2}}{V_2} = \frac{-s*C*R}{1+s*C*R}$$

V_{OUT}:

$$V_{OUT} = \frac{1}{1+s*C*R}V_1(s) - \frac{s*C*R}{1+s*C*R}V_2(s)$$

D. Passband centric design approach example

This section illustrates a passband centric design approach to building a five-stage filter.

The number of stages in equals 5.
Using the normalized bandwidth and number of stages, the spacing of the notch frequency (k) depends upon::

$$k = \frac{4}{5 - 1.3} * \ln\left(\frac{4.86 * \left(\sqrt[4]{5} - 1\right)}{0.85}\right) + 1 = 2.346$$

Next, the equation for estimating edge stop-band attenuation determines the approximate gain of the system

$$Edge\ Lobe\ Attenuation = 84.13 * 2.346^{-1.344} = 26.74\ dB$$

The equation for pass-band gain determines overall filter gain for positive frequency input:

$$\begin{aligned} Pass - band\ gain\ (odd) &= 20\log_{10}\sqrt{2} \\ &+ 40\sum_{l=1}^{\frac{N-1}{2}} \log_{10}\frac{k^l + 1}{\sqrt{k^{2l} + 1}} = 20\log_{10}\sqrt{2} + 40\sum_{l=1}^{\frac{5-1}{2}} \log_{10}\frac{2.346^l + 1}{\sqrt{2.346^{2l} + 1}} \\ &= 10.346\ dB \end{aligned}$$

The equation for k and passband gain found in Hay [19] and used in this design example.

Standard capacitor values and the general equation for RC time constant determine the values found in Table 16. The individual stage frequencies center at 3 kHz and use the ratio of *k to* determine adjacent frequencies.

Table 16. Component values selected in passband centric design approach

Stage	Notch Frequency (Hz)	Component Values	
		Standard 1% Capacitor (nF)	Standard 1% Resistor (kΩ)
1	2.448k	1	64.9/130
2	5.746k	1	28/56.2
3	13.482k	1	11.8/23.7
4	1.044k	10	15/30.1
5	445	10	35.7/71.5

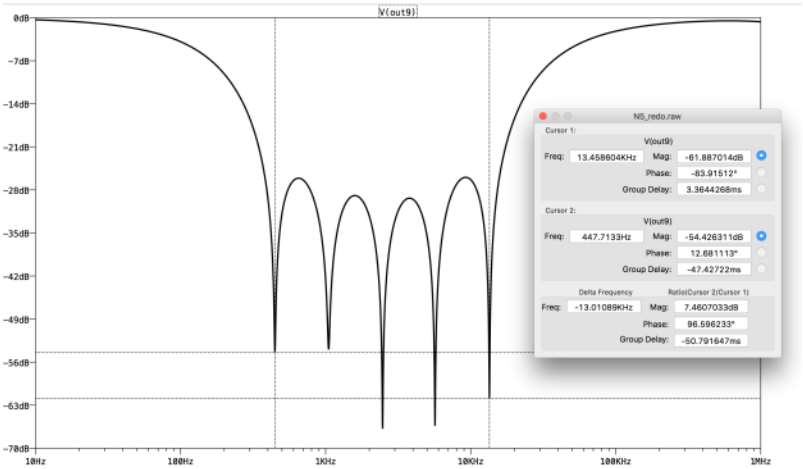

Figure 81. Stopband performance for topology with N = 5 and k = 2.346

Attenuation bandwidth: 13.01 kHz
Attenuation “floor”: 26.1 dB

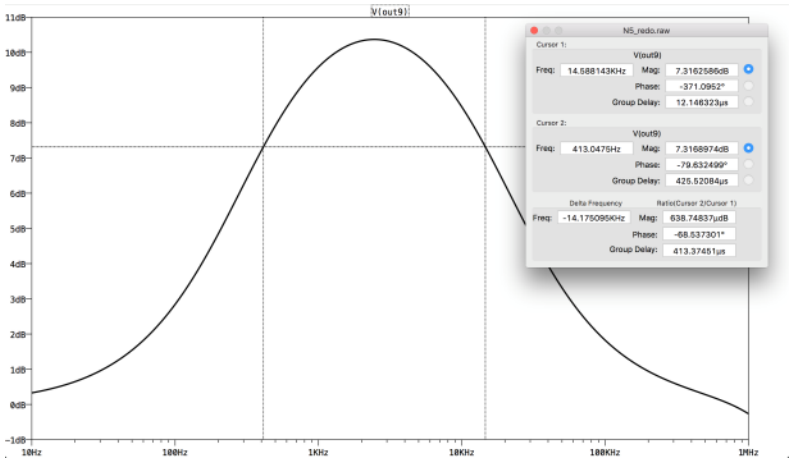

Figure 82. Passband performance when N = 5 and k = 2.346

Band-pass bandwidth: 14.175 kHz
Band-pass gain: 10.36 dB

After simulation, KICAD tools lay out the topology as a PCB.

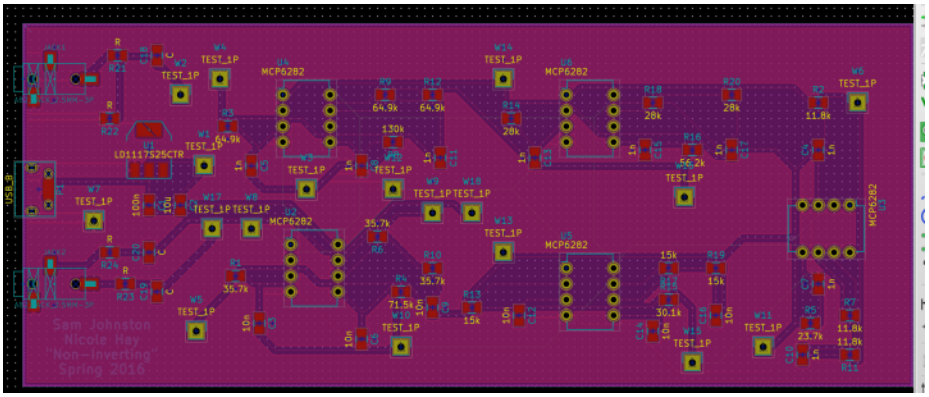

Figure 83. PCB layout of "Non-Inverting" topology when N = 5 and k = 2.346

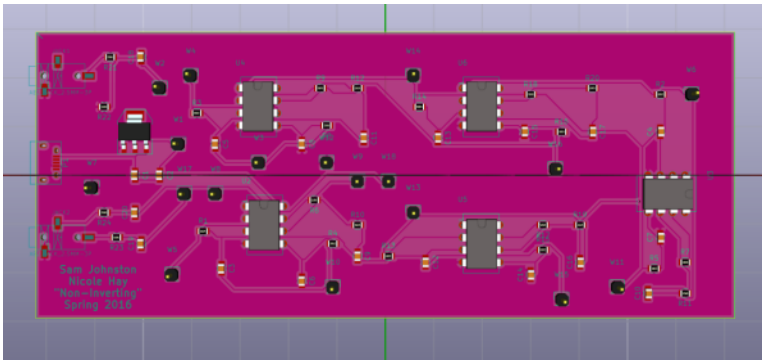

Figure 84. 3D view of PCB layout of "Non-Inverting" topology where N = 5 and k = 2.346